Calcium-sensitive subthreshold oscillations and electrical coupling in principal cells of mouse dorsal cochlear nucleus

Hong H[1,3] (洪卉), Moore LA[2,3], Apostolides PF[2], Trussell LO[1]

[1]Oregon Hearing Research Center and Vollum Institute and [2]Neuroscience Graduate Program, Oregon Health & Science University, Portland, Oregon 97239

[3]Co-first authors

Abbreviated title: Oscillations and electrical coupling in mouse DCN

Correspondence should be addressed to Laurence O. Trussell, trussell@ohsu.edu,

3181 SW Sam Jackson Park Road, L335A, Portland, OR 97239

47 Pages, 9 Figures, 1 extended data table

Number of words: 229 (Abstract), 531 (Introduction), 1477 (Discussion)

Acknowledgements: This work was supported by National Institutes of Health Grants DC004450 to L.O.T. and DC015187 to L.A.M. We thank Dr. Gideon Rothschild and members of the Trussell laboratory for helpful discussions and Sean Elkins, Jennifer Goldsmith, Ruby Larisch, and Michael Bateschell for assistance with mouse colony management. Current address for LAM is Masonic Institute for the Developing Brain, Institute of Child Development, College of Education and Human Development, University of Minnesota, Minneapolis, MN 55414. Current address for PFA is Kresge Hearing Research Institute & Department of Otolaryngology, University of Michigan, Ann Arbor, MI 48109.

Competing interests: None.

ABSTRACT

In higher sensory brain regions, slow oscillations (0.5-5 Hz) associated with quiet wakefulness and attention modulate multisensory integration, predictive coding, and perception. Although often assumed to originate via thalamocortical mechanisms, the extent to which sub-cortical sensory pathways are independently capable of slow oscillatory activity is unclear. We find that in the first station for auditory processing, the cochlear nucleus, fusiform cells from juvenile mice (of either sex) generate robust 1-2 Hz oscillations in membrane potential and exhibit electrical resonance. Such oscillations were absent prior to the onset of hearing, intrinsically generated by hyperpolarization-activated cyclic nucleotide-gated (HCN) and persistent Na^+ conductances (NaP) interacting with passive membrane properties, and reflected the intrinsic resonance properties of fusiform cells. Cx36-containing gap junctions facilitated oscillation strength and promoted pairwise synchrony of oscillations between neighboring neurons. The strength of oscillations were strikingly sensitive to external Ca^{2+}, disappearing at concentrations > 1.7 mM, due in part to the shunting effect of small-conductance calcium-activated potassium (SK) channels. This effect explains their apparent absence in previous *in vitro* studies of cochlear nucleus which routinely employed high-Ca^{2+} extracellular solution. In contrast, oscillations were amplified in reduced Ca^{2+} solutions, due to relief of suppression by Ca^{2+} of Na^+ channel gating. Our results thus reveal mechanisms for synchronous oscillatory activity in auditory brainstem, suggesting that slow oscillations, and by extension their perceptual effects, may originate at the earliest stages of sensory processing.

SIGNIFICANCE STATEMENT (120 words max.)

Many studies show that electrical activity in higher brain regions is regulated by brain oscillations. Here we show that such oscillatory activity can arise even in the first levels of auditory processing in the cochlear nucleus of the brainstem (fusiform cells), and is generated not by neural networks but by the biophysical properties of individual neurons. Oscillations are highly sensitive to external Ca^{2+} due to interplay of multiple ionic conductances. Gap junctions between cells allows for amplification and synchrony of such activity. Oscillations are absent in pre-hearing neurons, suggesting that sound activity might be important for their emergence. We propose that such early-level oscillations may serve to enhance signaling associated with particular environmental stimuli.

INTRODUCTION

Oscillatory activity in the brain occurs at the single neuron and population level, typified by a rhythmic modulation of intracellular membrane potentials and extracellular local field potentials, respectively (Lagier et al., 2004; Okun et al., 2010; Hong et al., 2022). Distinct oscillation frequency bands seem to correlate with distinct brain states and arousal levels (Buzsáki, 2006), such that specific oscillation bands may promote coherent population activity, enable neurons to respond optimally to inputs of a certain frequency, and facilitate synaptic plasticity (Huerta and Lisman, 1995; Hutcheon and Yarom, 2000; Buzsáki and Draguhn, 2004; Lee et al., 2018).

In sensory cortices, slow oscillations in the 0.5-5 Hz band are particularly associated with deep sleep, quiet wakefulness (Crochet and Petersen, 2006; Poulet and Petersen, 2008) and

correlate with stimulus familiarity (Kissinger et al., 2018) as well as perceptual decisions (Einstein et al., 2017). In the auditory system, these slow oscillations are proposed to modulate cellular and circuit excitability (Lakatos et al., 2005) and amplify sensory inputs (Lakatos et al., 2007). Indeed, recent studies in mice and humans suggest that the relative phase of slow oscillations modulates the neural discrimination and perceptual detection of sound features (Henry et al., 2016; Guo et al., 2017), with slow oscillations predictively entraining to subthreshold rhythmic sounds to enable faster perception (Lawrance et al., 2014; ten Oever et al., 2014, 2017). Altogether, these previous studies suggest that slow oscillations dynamically influence the excitability of higher-order sensory circuits, such that understanding the origin and mechanistic bases of slow oscillations could identify fundamental determinants of sensory perception.

Although not fully understood mechanistically, slow oscillations are generally assumed to originate via intracortical or thalamo-cortical interactions (Sanchez-Vives & McCormick, 2000; Beltramo et al., 2013; Neske, 2016). By contrast, whether slow oscillations can be independently generated by sensory circuits below the thalamus has received little attention. We recently showed that in auditory efferent neurons of the brainstem, intrinsic ion channel properties are sufficient to drive membrane oscillations that lead to infra-slow (~0.1 Hz) bursting activity of the neuron (Hong et al., 2022). Here we show a different pattern of slow oscillatory activity (1-2 Hz) in the auditory brainstem that occurs in the first station of auditory afferent pathway. Using patch-clamp electrophysiology in acute brain slices of mouse auditory brainstem, we found that the principal output neurons (fusiform cells) of the dorsal cochlear nucleus (DCN) display large, spontaneous, and highly regular 1-2 Hz membrane potential

89 oscillations. Such oscillations are absent before hearing onset. Pharmacology revealed that
90 these oscillations are generated by the interplay of two ionic conductances, the
91 hyperpolarization-activated cyclic nucleotide-gated channels (HCN) and tetrodotoxin-sensitive
92 Na^+ channels. In exploring why such oscillations have not been previously reported in brain slice
93 studies, we found that they were acutely sensitive to external Ca^{2+} concentration over the
94 range used in standard *in vitro* studies, and disappeared in concentrations greater than 1.7 mM.
95 Finally, due to the electrical coupling between fusiform cells, subthreshold oscillations were
96 strengthened and synchronized between nearby neurons, and this coupling and synchrony
97 appeared to be confined to fusiform cells within single tonotopic domains. These results have
98 significant implications for our understanding of the initiation and propagation of oscillatory
99 activity throughout the central nervous system.
100

101 **MATERIALS AND METHODS**

102 **Animals**

103 All animal procedures were approved by Oregon Health & Science University's
104 Institutional Animal Care and Use Committee. Mice of postnatal (P) days 16-25 were used from
105 WT *C57BL/6*, heterozygous GlyT2-EGFP (*FVB.Cg- Tg(Slc6a5-EGFP)13Uze/UzeBsiRbrc*,
106 RRID:IMSR_RBRC04708; Zeilhofer et al. 2005), Thy1-YFP (*B6;CBA-Tg(Thy1-YFP)GJrs/GfngJ*,
107 RRID:IMSR_JAX:014130; Feng et al. 2000), Vglut2-IRES-Cre (*Slc17a6tm2(cre)Lowl/J*, RRID:
108 IMSR_JAX:016963; Vong et al., 2011), Ai9 tdTomato reporter (*B6.Cg-Gt(ROSA)26Sortm9(CAG-*
109 *tdTomato)Hze/J*, RRID:IMSR_JAX:007909; Madisen et al., 2010), and connexin36 KO (Hormuzdi
110 et al., 2001) of both sexes. To study the development of oscillations, P8-9 WT mice were used.

111 Fusiform cells are easily identifiable in slice preparations by their morphology and input
112 resistance, but the GlyT2-EGFP and Thy1-YFP genetic lines were used to more efficiently
113 visualize deeper cells and distinguish them from other cell types, particularly in older mice.
114 Specifically, the Thy1-YFP line labeled fusiform cells, while the GlyT2-EGFP line allowed us to
115 avoid the extremely numerous glycinergic interneurons of DCN surrounding the fusiform cells.
116 In some experiments, offspring of Vglut2-IRES-Cre and Ai9 tdTomato crosses were used. No
117 differences were observed in the properties of fusiform cells among these different mouse
118 lines.

119 **Brain-slice preparation**

120 Mice were decapitated under deep isoflurane anesthesia. Coronal slices (300 µm for
121 P16-25 mice, 210 µm for P8-9 mice) were cut on a vibratome (Leica VT1200S and Campden
122 Instruments 7000smz-2). Slices containing DCN were cut at a 30° ventral-dorsal angle (to
123 preserve electrical coupling of fusiform cells) in warm (~35°C) artificial cerebrospinal fluid
124 (ACSF). We were unsuccessful in finding electrically coupled fusiform cell pairs when slices were
125 cut in the sagittal plane (n=11 dual recordings; data not shown). ACSF contained (in mM) 130
126 NaCl, 2.1 KCl, 1.2 KH_2PO_4, 1.7 $CaCl_2$, 1 $MgSO_4$, 20 $NaHCO_3$, 3 Na-HEPES, 10-12 glucose, 2 Na-
127 pyruvate, and 10 µM MK-801 and was bubbled with 5% CO_2/95% O_2 (300-310 mOsm). Slices
128 recovered for 30 min at 34°C and were then kept at room temperature until use.

129 **Electrophysiology**

130 Slices containing DCN were held in a chamber perfused with ACSF at a rate of 2-3
131 ml/min and heated to 30-33°C with an in-line heater. Neurons were visualized with Dodt
132 contrast optics using 10X and 40X objectives on an upright microscope (Zeiss Axioskop2). A

133 Multiclamp 700B amplifier was used to obtain whole-cell patch-clamp recordings from fusiform
134 cells. Data were filtered at 10 kHz, digitized at 20-50 kHz with a Digidata 1322A, or at 100 kHz
135 with a Digidata 1440A, and acquired with pClamp 10.4 software (Molecular Devices,
136 RRID:SCR_011323). Except for the data in Figure 1D, oscillations were recorded in the presence
137 of synaptic blockers to reduce signal variance and optimize cross-correlation analysis, including
138 5-10 µM NBQX, 10 µM MK-801, 0.5-1 µM strychnine, and 5-10 µM SR-95531.

139 For experiments in which the bath Ca^{2+} concentration was varied, the total
140 concentration of divalent ions was held constant at 2.7 mM by addition of Mg^{2+} to the ACSF.
141 ACSF of each Ca^{2+} concentration contained (in mM) 130 NaCl, 3 Na-HEPES, 20 $NaHCO_3$, ~7
142 glucose, 0.05 $NiCl_2$, 0.05 $CdCl_2$, 0.4 ascorbate, and 2 Na-pyruvate. ACSF of varying Ca^{2+}
143 concentrations were mixed from stock solutions containing either 2.6 mM Mg^{2+} or 2.6 mM Ca^{2+}.
144 The Mg^{2+} stock solution contained, along with the above, 1 $MgSO_4$, 1.6 $MgCl_2$, and 3.3 KCl, and
145 the Ca^{2+} stock solution contained 2.6 $CaCl_2$, 1 K_2SO_4, and 1.3 KCl. KCl replaced KH_2PO_4 in order
146 to prevent precipitation of Ca^{2+} (Kim and Trussell, 2007). HCN conductance in varying
147 concentrations of Ca^{2+} was measured in a total divalent concentration of 2.8 mM in order to
148 include 0.2 mM $BaCl_2$.

149 The majority of experiments were performed with a K-gluconate internal pipette
150 solution containing, in mM: 113 K-gluconate, 4.5 $MgCl_2$, 0.1 EGTA, 9 HEPES, 14 tris-
151 phosphocreatine, 4 Na_2-ATP, 0.3 tris-GTP, with pH adjusted to 7.25 with KOH and osmolality
152 adjusted to 290 mOsm with sucrose. In some experiments, 4.5 mM $MgCl_2$ were replaced by
153 2.75 mM $MgCl_2$ and 1.75 mM $MgSO_4$. Membrane potentials measured using the K-gluconate
154 pipette fill were adjusted for a junction potential of -13 mV. Input resistance was measured by

155 injecting a -10-pA current into the fusiform cell in current-clamp mode. A Cs-TEA internal was
156 used to measure persistent Na^+ (NaP) conductance. This internal solution contained (in mM)
157 115 TEA-Cl, 4.5 $MgCl_2$, 3.5 CsCl, 10 EGTA, 10 HEPES, 4 Na_2-ATP, 0.5 tris-GTP, 5 CsOH to adjust pH
158 to 7.25, and 15 sucrose to adjust osmolality to 290 mOsm. Results from experiments using this
159 solution were corrected for a junction potential of -3 mV. Recording electrodes of 4-6 MΩ were
160 pulled from borosilicate glass (WPI 1B150F-4) with a vertical puller (Narishige P-10). For
161 voltage-clamp recordings, series resistance (<20 MΩ) was compensated by 60-80% correction
162 and 90% prediction with the Multiclamp 700B (bandwidth 3 kHz). Data were only included for
163 final analysis if the series resistance changed by <20% over the course of the experiment.
164 Reagents were purchased from Sigma-Aldrich and Alomone Labs.

165 **Frequency-domain analysis**

166 The power spectrum for spontaneous oscillations (binned at 0.1-0.2 Hz) was generated
167 in Clampfit analysis software (version 10.9, Molecular Devices) from 20-30 s segments of
168 representative traces using a Hamming window 50% overlap of spectral segments. The
169 resonant frequency of neurons was determined by injecting a 5 pA swept sine wave (ZAP, or
170 impedance (*Z*) amplitude profile) current that varied in frequency from 0 to 10 Hz over 20
171 seconds (Puil et al., 1986). Neurons were injected with negative bias current just sufficient to
172 prevent spiking during the ZAP current injection and spontaneous oscillation frequency and
173 power were measured at this same holding potential. ZAP current was run for 20-50 trials for
174 individual neurons and the voltage responses were averaged. Based on code from Bakken et al.,
175 (2021), impedance (*Z*) was calculated from the ratio of the fast Fourier transforms of measured
176 voltage response (*V*) and the injected current (*I*):

177

178 $$Z = \frac{FFT(V)}{FFT(I)}$$

179

180 For a resonant neuron, the resulting impedance curve displays a peak in impedance at the
181 resonant frequency. A smoothing protocol was applied to reduce flutuations in the impedance
182 curve (Fig. 4B), and measurements of resonance peak made from the smoothed trace. The
183 height of this peak is quantified by the Q value, which here is the peak impedance value divided
184 by the impedance value measured at 0.4 Hz.

185 **Conductance measurements**

186 To measure NaP activation, a ramp was delivered to the neuron from -83 to -53 mV over
187 the course of 5 seconds (Leao et al., 2012). 1-10 nM TTX was included in the bath to help
188 suppress escaping spikes and therefore enable current measurements at more depolarized
189 potentials. Cd^{2+}/Ni^{2+} (50 µM each) were included in the bath to block calcium channels. The first
190 ~2 seconds of the response was dominated by a linear outward current reflecting the passive
191 membrane response to the voltage ramp. We fit this with a line and subtracted the linear
192 values from the current response to perform leak subtraction. In a subset of experiments, a
193 ramp from -83 to -3 mV over the course of 6 seconds was applied to the neuron. After
194 recording the current response to this ramp, TTX (1 µM) was applied in the bath and the ramp
195 was repeated. The current traces after TTX were subtracted from those before TTX, in order to
196 isolate TTX-sensitive NaP current. These experiments were conducted with either 1.7 or 2.5
197 mM Ca^{2+}. The results from the two voltage ramp protocols were consistent (see *RESULTS*). To
198 analyze the voltage dependence of NaP activation, conductance (*G*) was calculated according to

199 the following equation, where *I* is current measured at a given voltage (*V*), and *Vrev* is the

200 reversal potential of Na^+ (calculated to be +77.4 mV):

201

202 $$G = \frac{I}{(V - Vrev)}$$

203

204 HCN activation in different external Ca^{2+} concentrations was measured similar to Tang &

205 Trussell (2015). Cells were held at -60 mV and 5-second steps from -120 to -60 mV were applied

206 in 5-mV increments. After each 5-second step, the cell was brought back to -60 mV, resulting in

207 a tail current from which HCN activation could be approximated. The bath solution included

208 Cd^{2+}/Ni^{2+} (50 µM each) to block Ca^{2+} currents, and TTX (0.5 µM) to block Na^+ current. Ba^{2+} (0.2

209 mM) and 4-aminopyridine (4-AP; 1 mM) were also included to reduce contamination in the tail

210 current from leak conductance and low-voltage activated K^+ channels respectively (Johnston et

211 al., 2010; Leao et al., 2012). Both drugs slightly block HCN channels at these concentrations

212 (Ludwig et al., 1998).

213 The resulting NaP and HCN activation curves were fit with a Boltzmann equation:

214

215 $$y = base + \frac{(max - base)}{1 + exp\left(\frac{v50 - x}{slope}\right)}$$

216

217 The *base* value was set to 0. The other resulting values, *max* (maximum conductance), *v50*

218 (half-activation voltage of the curve), and *slope* (a value that describes the steepness of the

219 sigmoid) were compared for each cell between different external Ca^{2+} concentrations. The

220 population conductance curves for NaP and HCN were generated by normalizing raw
221 conductance values for each cell to the *max* value given by the Boltzmann fit. These average
222 values were then fit with their own Boltzmann equation.

223 **Paired recordings and cross-correlation analysis**

224 The coupling coefficient for electrically coupled fusiform cells was determined by
225 holding both cells in current clamp and alternating injection of a -1 nA square pulse into each
226 cell. Coupling coefficient was calculated by dividing the amplitude of the voltage deflection in
227 the post-junctional cell by the amplitude of the voltage deflection in the pre-junctional cell.
228 Pairs were considered to be coupled if the coupling coefficient was greater than 0.005 (Yaeger
229 and Trussell, 2016).

230 For cross-correlation analysis for cell pairs, 1-2 min segments of subthreshold traces
231 with a steady baseline were selected. Traces were resampled from 50 to 200 µs inter-sample-
232 interval, bandpass filtered at 0.2-10 Hz, and baseline-subtracted. Cross-correlograms were
233 generated in Igor and normalized by dividing cross-correlation coefficient values (xcorr) by the
234 standard deviation (sd) of each trace multiplied together:

235

236 $$\text{normalized xcorr}(t) = \frac{\text{xcorr}(t)}{\text{sd}\big(\text{A}(t')\big) * \text{sd}(\text{B}(t'))}$$

237

238 where xcorr(t) is the raw cross-correlation coefficient calculated for a given lag time t, and A(t')
239 and B(t') are the voltage traces with t' representing the time variable for the traces. In this way,
240 if the analysis were an auto-correlation, variance would be the normalization factor and the
241 value at time zero would be 1 (Beierlein et al., 2000).

242 For spike cross-correlation, spikes were detected using threshold search in Clampfit,
243 generating a list of spike times for each cell. Spike times were binned in 1- and 10-ms segments
244 and cross-correlated in Igor. Resulting cross-correlation coefficients (xcorr) were then adjusted
245 and normalized according to the following equation:
246

247 $$\text{normalized xcorr}(t) = \frac{\text{xcorr}(t) - \text{scrambled}}{\sqrt{n_A * n_B}}$$

248

249 where n_A and n_B are spike counts from traces A and B. The *scrambled* term is the average cross-
250 correlation coefficient value from cross correlating spikes from trace A with scrambled spike
251 times from trace B, generated using the *random.shuffle* function in Python. This is used in place
252 of the theoretically calculated term used by others (Eggermont, 1992; Stefanescu and Shore,
253 2015). In the text, both oscillation and spike time cross-correlation coefficient values are
254 referred to as *xcorr* for simplicity. Peak *xcorr* values reported are measured at zero lag instead
255 of the real peak.

256 **Experimental design and statistical analysis**

257 Electrophysiological traces were analyzed with pClamp 10.4 software or custom-written
258 procedures in IGOR Pro 6.3 or 8.04 (RRID:SCR_000325) and Python 2.6 (RRID:SCR_008394). For
259 spike shape analysis in Extended Data Table 2-1, spike threshold was defined as voltage at the
260 time point when spike dV/dt reached 5% of its peak. GraphPad Prism 7 and 9
261 (RRID:SCR_002798) was used for statistical analysis and to make figures. Data are represented
262 in the text and figures as mean ± SEM. Parametric analysis was used only after confirming
263 assumptions of equal variances (F test for two-group comparison and Bartlett's test for three-

264 group comparison) and normality (D'Agostino-Pearson omnibus normality test). The equivalent
265 non-parametric tests were used when data were not normal; the name of the test used is
266 included with all statistics reported in the *RESULTS* section. One-way ANOVA with repeated
267 measures (RM) was used to compare statistics for single cells across more than two conditions,
268 followed by Tukey's *post hoc* comparisons (p values associated with post hoc tests are only
269 reported when the main effect is significant). The Geisser and Greenhouse correction was
270 applied to RM one-way ANOVAs to correct for possible violations of the assumption of
271 sphericity (of note, this frequently changes associated degrees of freedom values to non-
272 integers). Assumptions of sphericity and effective matching were also confirmed for one-way
273 ANOVAs.
274
275 **RESULTS**
276 **Fusiform cell membrane potential oscillates at rest**
277 In acute DCN brain slices, approximately 80% of patched fusiform cells displayed 1-2 Hz
278 subthreshold oscillations around the resting membrane potential in the absence of ongoing
279 spike activity (Fig. 1A). Power spectrum analysis of the oscillations revealed a clear peak in this
280 frequency range, averaging 1.10 ± 0.03 Hz over the population (n=128 cells; Fig. 1B,E).
281 Oscillation power was strongly voltage-dependent, indicating the involvement of voltage-
282 sensitive channels (Fig. 1C; n=10 cells). Oscillations were typically recorded in the presence of
283 blockers of fast synaptic transmission (see *MATERIALS AND METHODS*), but were also clearly
284 present in the absence of synaptic blockers (Fig. 1D). Synaptic blockers slightly reduced the
285 oscillation frequency (Fig. 1E; control: 1.50 ± 0.08 Hz, n=28 cells; synaptic blockers: 1.10 ± 0.03

286 Hz, n=128 cells; U=845, p<0.0001, Mann-Whitney U) but increased the oscillation power (Fig.
287 1F; control: 0.8 ± 0.1 mV^2/Hz, n=26 cells; synaptic blockers: 3.5 ± 0.5 mV^2/Hz, n=128 cells;
288 U=862, p<0.0001, Mann-Whitney U). The increase in power with blockers was paralleled by an
289 increase in input resistance (Fig. 1G, left; control: 164.8 ± 18.8 MΩ, n=13 cells; synaptic
290 blockers: 240.9 ± 20.8 MΩ, n=22 cells; t(33)=2.478, p=0.019, two-tailed t-test), reflecting the
291 loss of the shunting effect of spontaneous synaptic activity. Accordingly, membrane time
292 constant (tau) increased upon block of synaptic activity (Fig. 1G, right; control: 23.56 ± 2.02 ms;
293 synaptic blockers: 35.54 ± 2.06 ms; t(33)=3.860, p=0.0005, two-tailed t-test), while membrane
294 capacitance did not change (Fig. 1G, middle; U=135, p=0.8, Mann-Whitney U).

295

296 **Oscillations are absent in fusiform cells from pre-hearing mice**

297 We next asked whether the presence of oscillations reflected an electrically immature
298 state of fusiform cells by recording from younger neurons, specifially choosing ages (P8-9)
299 before hearing onset. None of the fusiform cells generated spontaneous action potentials (APs)
300 at these immature ages. Unlike older neurons, the majority of P8-9 fusiform cells (12 out of 13)
301 did not exhibit oscillations at rest (Fig. 2A). The power from auto-correlation analysis was below
302 0.1 mV^2/Hz for all the pre-hearing neurons, significantly smaller than that of P16-25 fusiform
303 cells (Fig. 2B; P8-9: 0.030 ± 0.007 mV^2/Hz; n=13 cells, U=11, p<0.0001, Mann-Whitney U).
304 Surprisingly, such profound changes in oscillation did not correlate with developmental changes
305 in passive membrane properties, as assessed with small hyperpolarizing steps (Fig. 2C; input
306 resistance: P8-9: 269.7 ± 17.87 MΩ, P16-21: 240.9 ± 20.75 MΩ, U=126, p=0.38; capacitance: P8-
307 9: 178.0 ± 12.75 pF, P16-21: 162.5 ± 12.84 pF, U=111, p=0.17; tau: P8-9: 46.44 ± 2.82 ms, P16-

308 21: 35.54 ± 2.06 ms, U=76.5, p=0.01, Mann-Whitney U). Besides oscillations, active properties
309 also changed with age. In 11 out 14 fusiform cells at P8-9, a delay to onset of spiking was
310 apparent, an effect often attributed to activation of A-type K^+ current (Fig. 2D, arrowhead,
311 Kanold and Manis, 1999). This delay was not observed at older ages (Fig. 2E). Fusiform cells
312 from these two age groups also showed significant differences in rheobase, AP threshold and
313 AP width (Extended Data, Table 2-1), suggesting changes in Na^+-channel expression. Taken
314 together, the parallel maturation of AP properties and oscillation strength with age suggests
315 that some developmentally regulated ion channels play a role in both.
316
317 **NaP and HCN conductances are required for oscillations**
318 Previous studies show that subthreshold oscillations can be generated by Na^+ channels
319 (i.e., NaP current), HCN and/or T-type Ca^{2+} channels (Mccormick and Pape, 1990; Hughes et al.,
320 2002; Fransén et al., 2004). We therefore explored whether these ion channels participate in
321 driving the oscillations in fusiform cells. First, addition of 0.5 µM TTX markedly reduced
322 oscillations, indicating a critical role for Na^+ channels (Fig. 3A; control: 6.1 ± 4.3 mV^2/Hz; TTX:
323 0.0052 ± 0.0009 mV^2/Hz; wash: 4.6 ± 3.4 mV^2/Hz; n=7 cells, W=11.14, p=0.0012, Friedman test).
324 Overall, 88% (22 out of 25) of fusiform cells recorded in TTX showed no oscillations. Second,
325 bath application of the HCN channel blocker Cs^+ (1-2 mM) also attenuated oscillation power
326 (Fig. 3B; control: 5.7 ± 1.8 mV^2/Hz; Cs^+: 0.2 ± 0.1 mV^2/Hz; wash: 4.6 ± 1.4 mV^2/Hz; n=10 cells,
327 F(1.2, 10.8)=8.7, p=0.01, RM one-way ANOVA). In a separate set of experiments, ZD7288 (10
328 µM) was applied to confirm the role of HCN channels in oscillations. ZD7288 had matching

329 effects to Cs^+ (control: 8.0 ± 3.9 mV^2/Hz; ZD: 0.4 ± 0.03 mV^2/Hz; n=6 cells, W=-21, p=0.03,

330 Friedman test).

331 We also tested for the involvement of K^+ channels. The non-specific K^+ channel blocker

332 TEA (10 mM) significantly increased oscillation power from 2.5 ± 1.9 to 13.7 ± 9.8 mV^2/Hz (Fig.

333 3C; wash: 2.0 ± 1.5 mV^2/Hz; n=7 cells, F=12.29, p=0.0003, Friedman test). This observation

334 suggests that K^+ channels activating at subthreshold voltages exert a shunting effect on

335 membrane oscillations, rather than driving the repolarization of the oscillatory cycle. Finally, we

336 tested the role of T-type Ca^{2+} channels, which are known to drive oscillatory activity in thalamus

337 (Steriade et al., 1993; Hughes et al., 2002). Surprisingly, we found that oscillations in fusiform

338 cells persisted in the presence of Ca^{2+} channel blockers: addition of broad-spectrum Ca^{2+}

339 channel blockers, 100 μM Cd^{2+} and 50 μM Ni^{2+}, resulted in a slight but non-significant increase

340 in oscillation power (Fig. 3D; control: 3.9 ± 1.5 mV^2/Hz; Cd^{2+}/Ni^{2+}: 7.2 ± 2.6 mV^2/Hz; wash: 4.6 ±

341 1.6 mV^2/Hz; n=6 cells, F(1.6,7.9)=4.64, p=0.052, RM one-way ANOVA). Ni^{2+} also blocks NMDA

342 receptors and therefore rules out the involvement of this conductance as well (Mayer and

343 Westbrook, 1985); the exposure of tissue to MK-801 during slice preparation further reduces

344 the likelihood of NMDA receptor involvement. Nevertheless, the slight increase in oscillation

345 power with Cd^{2+} and Ni^{2+} might be a result of indirect blockade of Ca^{2+}-activated K^+ channels,

346 thus suggesting the possibility of a tonic activation of Ca^{2+}-activated K^+ channels at resting

347 voltages. In a later section (Fig. 6), we demonstrate that this Ca^{2+}-activated K^+ channel is the

348 small-conductance calcium-activated potassium (SK) channel. Altogether, these results support

349 a model whereby oscillations are generated by the interplay between NaP and HCN

350 conductances, whereas K^+ channels negatively regulate the power of the oscillations.

351

352 **Fusiform cells show slow intrinsic resonance**

353 Resonance refers to the ability of a neuron to amplify voltage responses to current
354 stimuli over a narrow frequency range. To evaluate resonance, a frequency ramp (ZAP) is
355 delivered to the neuron and the frequency-dependent resistance (impedance, *Z*) is measured
356 across frequency (Hutcheon and Yarom, 2000); peak resonance corresponds to the peak in
357 impedance. Previous studies show a close association between oscillations and resonance, as
358 they may share underlying ion channel mechanisms (Hutcheon and Yarom, 2000). We explored
359 resonance in fusiform cells by injecting a ZAP from 0-10 Hz (Fig. 4A). The raw impedance trace
360 (Fig. 4B, grey trace) was smoothed (black trace) to identify the peak in the curve (dashed line,
361 see *MATERIALS AND METHODS*). All the fusiform cells exhibited a resonant peak in response to
362 the ZAP (n=19 cells; Fig. 4B). Notably, the frequency corresponding to the resonance peak was
363 not significantly different from their oscillation frequency (Fig. 4C; resonance: 1.21 ± 0.09 Hz;
364 oscillation: 1.23 ± 0.07 Hz; n=17 cells, t(16)=0.340, p=0.74, paired t-test). To characterize the
365 magnitude of resonance, impedance at the resonance peak was normalized to impedance at
366 0.4 Hz (Fig. 4D). The peak of the resulting curve is defined as Q (Fig. 4E). A non-resonant neuron
367 will have a Q value equal to 1. All fusiform cells measured had a Q value greater than 1, with an
368 average value of 1.55 ± 0.06 (n=17 cells, U=0, p<0.0001, Mann-Whitney U).

369 As NaP and HCN conductances play an essential role in generating oscillations in
370 fusiform cells, we next examined their roles in resonance. 1 mM Cs^+ abolished resonance in
371 fusiform cells (Fig. 4F), indicating a requirement for HCN channels in setting the resonance
372 peak. The resulting impedance curve decreased as the frequency increased, a characteristic of a

373 passive membrane (Fig. 4F, lower panel). For normalized impedance curves in the presence of
374 Cs^+ for each cell, we measured impedance value at the frequency corresponding to the
375 resonance peak in control solutions. The average of this Q-for-drug value was 0.96 ± 0.03, not
376 significantly different from 1 (Fig. 4H, left; n=6 cells, U=12, p=0.364, Mann-Whitney U). In
377 addition, a "Z ratio" was calculated as the un-normalized impedance with Cs^+ (again, measured
378 at the resonance frequency determined in control) divided by the peak impedance in control, a
379 metric that reflects both the changes in resonance and overall impedance induced by Cs^+. On
380 average, Z ratio was 0.53 ± 0.10 with Cs^+ (Fig. 4I, left; n=6 cells).
381 TTX (0.5-1 µM) also attenuated the resonance of fusiform cells (Fig. 4G). Q in TTX was
382 significantly smaller than control values (Fig. 4H, right; control: 1.70 ± 0.11; TTX: 1.17 ± 0.04;
383 n=7 cells, t(6)=5.796, p=0.0012, paired t-test). Z ratio was 0.46 ± 0.06 in TTX (Fig. 4I, right).
384 Different from what was observed with Cs^+, however, neurons in TTX still maintained some
385 residual resonance (Fig. 4G, lower panel), as the Q for TTX was significantly larger than 1 (U=0,
386 p=0.0006, Mann-Whitney U), and larger than Q for Cs^+ (Fig. 4H; t(11)=4.049, p=0.0019, two-
387 tailed t-test). Taken together, HCN current is essential for resonance in fusiform cells, while NaP
388 contributes to its amplification. These results show that oscillations are an outcome of the
389 intrinsic resonance properties of fusiform cells generated by their complement of ion channels.
390

391 **External Ca^{2+} concentration determines the strength of oscillations**

392 The presence of oscillations in fusiform cells was surprising given that they had not been
393 reported, despite decades of studies of these cells *in vitro* (Manis, 1990; Gardner et al., 2001;
394 Fujino and Oertel, 2003; Manis et al., 2003; Tzounopoulos et al., 2004). However, most previous

395 studies of fusiform cells used an external Ca^{2+} concentration of 2.4-2.5 mM (Gardner et al.,
396 2001; Fujino and Oertel, 2003; Manis et al., 2003; Tzounopoulos et al., 2004). Our experiments
397 thus far used 1.7 mM Ca^{2+}, closer to the external Ca^{2+} concentration of CSF *in vivo* (Somjen
398 2004; Borst, 2010). Might differences in external Ca^{2+} explain why other studies did not report
399 oscillations in fusiform cells? We tested this hypothesis by systematically determining the
400 relation between oscillation power and Ca^{2+}. Oscillation strength showed a remarkably steep
401 dose-dependence on Ca^{2+} concentration, decreasing to undetectable levels above 2 mM Ca^{2+},
402 with a half-maximal power at 1 mM (Fig. 5A-C, n=8 cells). Though 1.7 and 2.5 mM are on the
403 tail-end of the dose-response curve, there is a >4 fold difference between power
404 measurements in these two concentrations. Indeed, both raw and normalized power
405 measurements show that power measured at 1.7 mM was significantly larger than power
406 measured at 2.5 mM Ca^{2+} (U=-36, p=0.008, Mann-Whitney U, also see Fig. 6E). Figure 5C shows
407 that oscillation power of a representative fusiform cell changed over time when external Ca^{2+}
408 was switched between 1.7 and 0.5 mM. The interval between two consecutive data points is 30
409 seconds. The effect of Ca^{2+} was rapid: within three minutes of washing in 0.5 mM Ca^{2+}, there
410 was a pronounced increase in power, while the power quickly returned to its initial value when
411 1.7 mM Ca^{2+} was re-applied. Such increase in oscillation power is not due to altered input
412 resistance, which was not significantly different between 1.7 and 0.5 mM Ca^{2+} (average(1.7 and
413 0.5 mM Ca^{2+})=114.3 ± 11.8, 115.4 ± 17.0 MΩ, n=5 cells, t(4)=0.082, p=0.939, paired t-test).
414 The experiments described in Figure 3 highlight the critical role of Na^{+} and HCN
415 channels in the genesis of the oscillations. Interestingly, previous studies showed that external
416 Ca^{2+} concentration regulates the voltage sensitivity of Na^{+} channels, with lower concentrations

417 causing a negative shift in the half-activation voltage (Frankenhaeuser and Hodgkin, 1957;
418 Campbell and Hille, 1976). It may be that lowering external Ca^{2+} could activate more NaP
419 current, contributing to a greater amplification of oscillations. We therefore tested whether
420 changes in Ca^{2+} concentration over the range that modulates oscillation strength would also
421 affect Na^{+} current in fusiform cells. NaP conductance was measured in voltage clamp by
422 gradually ramping membrane potential from -83 to -53 mV over the course of 5 seconds (Fig.
423 5D; Leao et al. 2012). Voltage control was maintained by limiting Na^{+} current amplitude with a
424 submaximal dose of TTX, by blocking background currents, and by using a narrow range of
425 voltages. In this experiment, we used three Ca^{2+} concentrations, 0.5, 1.7 and 2.5 mM,
426 representing low, moderate and high Ca^{2+}, respectively. The amplitude of NaP current at
427 individual membrane voltages was measured and transformed to conductance, which was
428 further plotted as a function of membrane voltage. A Boltzmann function was fitted to the
429 resulting curve in order to calculate the maximum conductance, half-maximal activation voltage
430 (*v50*) and slope factor (see *MATERIALS AND METHODS*). Figure 5E shows normalized
431 conductance curves from a representative neuron to illustrate the difference in *v50*. *V50*
432 displayed a significant positive shift in higher Ca^{2+} concentrations (Fig. 5F, middle; n=9 cells,
433 F(1.7, 13.3)=31.07, p<0.0001, RM one-way ANOVA): *v50* shifted from -61.2 ± 1.0 mV in 0.5 mM
434 to -56.5 ± 1.0 mV in 1.7 mM (p<0.0001) and -56.9 ± 1.3 mV in 2.5 mM (p=0.001). However, *v50*
435 was not measurably different between 1.7 and 2.5 mM conditions (p=0.851). Maximum
436 conductance, as predicted by the Boltzmann fits, was not different between conditions,
437 averaging 3.1 ± 0.7, 3.6 ± 0.8, and 2.7 ± 0.7 nS from low to high concentration (Fig. 5F, left; n=9
438 cells, F(1.2, 9.9)=1.6, p=0.239, RM one-way ANOVA). Slope was also unchanged between all

439 conditions, averaging 3.0 ± 0.2, 3.2 ± 0.2, and 3.0 ± 0.2 nS/mV in 0.5, 1.7, and 2.5 mM Ca^{2+} (Fig.
440 5F, right; n=9 cells, F(1.1, 9.0)=0.514, p=0.514, RM one-way ANOVA). To further explore an
441 effect of Ca^{2+} on Na^{+} currents in higher Ca^{2+}, in a subset of experiments a wider-range voltage
442 ramp from -83 to -3 mV over the course of 6 seconds was applied to fusiform cells with 1.7 and
443 2.5 mM Ca^{2+}. Consistently, *v50* was not significantly different (1.7 mM Ca^{2+}: -56.5 ± 1.4 mV, n=6
444 cells; 2.5 mM Ca^{2+}: -52.8 ± 1.0 mV, n=5 cells; t(9)=2.019, p=0.074, two-tailed t-test). In
445 summary, increasing external Ca^{2+} concentration in the range from 0.5 to 1.7 mM effectively
446 decreased NaP conductance to inhibit oscillations by positively shifting the half-maximal
447 activation voltage of the channels. However, further increases in external Ca^{2+}, which further
448 decreased oscillation power, had no measurable effect on the parameters of NaP conductance.
449 We next investigated what mediates the change in oscillation power between 1.7 and
450 2.5 mM Ca^{2+}. Figure 6A shows the time course of power change from a representative fusiform
451 cell. Similar to what was observed with 0.5 mM Ca^{2+}, fusiform cells also responded to 2.5 mM
452 Ca^{2+} in a rapid manner; within three minutes the power dropped below detectable levels, and
453 was restored by re-application of 1.7 mM Ca^{2+}. Interestingly, oscillations were preserved when
454 applying 2.5 mM Ca^{2+} along with TEA (Fig. 6A), suggesting that Ca^{2+}-activated K^{+} channels might
455 play a role in shunting the voltage change with high external Ca^{2+}. In line with this
456 interpretation, input resistance was significantly smaller with 2.5 mM Ca^{2+}, but such Ca^{2+}
457 dependence was abolished with 1 mM TEA in the bath (Fig. 6B; average(1.7, 2.5 mM Ca^{2+})=
458 295.2 ± 42.7, 179.5 ± 26.5 MΩ, n=7 cells, q(6)=6.997, p=0.006; average(1.7+TEA, 2.5 mM
459 Ca^{2+}+TEA)=208.1 ± 16.6, 177.1 ± 29.3 MΩ, n=6 cells, q(5)=2.121, p=0.367, Tukey's post hoc
460 test). Ca^{2+} dependence of oscillation power was also attenuated by TEA or 200 nM apamin to

461 specifically block SK channels. When switching from 1.7 to 2.5 mM Ca^{2+} with TEA or apamin in
462 the bath, oscillations were preserved (Fig. 6C,D). Although we still observed a significant
463 reduction in oscillation power with higher Ca^{2+}, the percent reduction is only ~55% with TEA
464 and ~56% with apamin, significantly smaller than ~95% reduction in control (Fig. 6E; control *vs.*
465 TEA, $q(16)=12.80$, $p<0.0001$; control *vs.* apamin, $q(16)=12.28$, $p<0.0001$, Tukey's post hoc test).
466 Taken together, elevation of bath Ca^{2+} concentration in the range used in previous brain slice
467 studies activated background SK channel conductance, thereby shunting voltage oscillations.
468 We also tested for possible effects of Ca^{2+} concentration on HCN conductance (Fig.
469 7A,B). Ca^{2+} concentration did not affect the maximum HCN tail current (Fig. 7C; average(0.5,
470 1.7, 2.5 mM Ca^{2+})=245.0 ± 21.5, 254.1 ± 23.8, 265.7 ± 19.7 pA, n=11 cells, $F(1.9,19.5)=1.61$,
471 $p=0.225$, RM one-way ANOVA), or the parameters of the Boltzmann equation, including *v50*
472 (Fig. 7C; average(0.5, 1.7, 2.5 mM Ca^{2+})=-92.8 ± 1.4, -92.8 ± 1.2, -92.2 ± 1.4 mV, n=11 cells,
473 $F(1.6, 15.9)=0.18$, $p=0.791$, RM one-way ANOVA) and slope (Fig. 7C; average(0.5, 1.7, 2.5 mM
474 Ca^{2+})=-7.6 ± 0.3, -7.5 ± 0.4, -7.5 ± 0.7 pA/mV, n=11 cells, $F(1.4, 14.3)=0.03$, $p=0.929$, RM one-
475 way ANOVA). These results indicate that extracellular Ca^{2+} sensitivity of fusiform cell oscillations
476 is attributed to the effect of Ca^{2+} on NaP and SK current, and explains why such slow oscillations
477 in fusiform cells has not been previously reported.
478 Given the effects of bath Ca^{2+} and of synaptic blockers reported above, we measured
479 the power of oscillations when ongoing synaptic events were present and bath Ca^{2+} held to a
480 physiological level of 1.2 mM. In the absence of synaptic blockers, the power in fusiform cells
481 was significantly larger than that with 1.7 mM Ca^{2+} (Fig. 1F, left; 1.7 Ca^{2+}: 0.764 ± 0.122, n=26

482 cells; 1.2 Ca^{2+}: 2.327 ± 0.662 mV^2/Hz, n=6 cells, U=19.50, p=0.0028, Mann-Whitney U),

483 indicating that oscillations are apparent under physiological conditions.

484

485 **Electrical coupling and oscillation synchrony**

486 Fusiform cells are electrically coupled via gap junctions. Although the probability of

487 neighboring fusiform cells being electrically coupled is high (around 70%, based on coupling

488 measured in 20/28 recorded cell pairs), the strength of coupling is low (coupling coefficient

489 ~0.01; Apostolides & Trussell, 2013). Interestingly, paired recordings from fusiform cells

490 revealed strong oscillation synchrony between neurons despite this apparent weak coupling.

491 Cross-correlograms obtained from cross-correlating the voltage signals of electrically coupled

492 pairs displayed a peak close to zero lag (Fig. 8A). To determine whether the oscillation

493 synchrony was indeed due to electrical coupling, we made dual recordings from Cx36 KO

494 animals in which electrical coupling in DCN is abolished (Apostolides and Trussell, 2013; Yaeger

495 and Trussell, 2016). Interestingly, although fusiform cells from Cx36 KO tissue still displayed

496 oscillations, there was no longer synchrony between closely apposed fusiform cells (Fig. 8B).

497 Population statistics are displayed in Figure 8C. The average *xcorr* for coupled pairs was 0.5 ±

498 0.05 (n=26 pairs). This was significantly larger than *xcorr* values for uncoupled pairs in WT and

499 Cx36 KO tissue, both of which were close to zero (Fig. 8C, left; 0.01 ± 0.01 (n=13 pairs) for

500 uncoupled WT and -0.01 ± 0.02 (n=10 pairs) for KO; $F(2,46)=49.6$, $p<0.0001$, one-way ANOVA;

501 post hoc WT *vs.* WT uncoupled $p<0.0001$, WT *vs.* Cx36 KO $p<0.0001$). Coupled pairs in WT tissue

502 displayed peaks in their cross-correlograms close to zero lag, averaging 10.5 ± 1.8 ms (Fig. 8C,

503 right). These results indicate that fusiform cell oscillations are generated by cell intrinsic

504 conductances, whereas the presence of electrical synapses allows synchrony across the
505 neuronal population (Long et al., 2002).
506 The oscillations observed in Cx36 KO mice had significantly lower power than
507 oscillations recorded from WT mice (Fig. 8D; averages WT: 3.7 ± 0.5 mV^2/Hz (n=117 cells), KO:
508 0.9 ± 0.3 mV^2/Hz (n=19 cells); U=405, p<0.0001, Mann-Whitney U). The frequency, however,
509 was unchanged (Fig. 8D; averages WT: 1.12 ± 0.03 Hz (n=117 cells), KO: 1.32 ± 0.12 Hz (n=19
510 cells); U=846, p=0.096, Mann-Whitney U). This result indicates that synchronization rendered
511 by electrical coupling likely acts to boost oscillation power.
512
513 **Electrical coupling and spike synchrony**
514 The presence of synchrony in subthreshold voltage oscillations might lead to spike
515 synchrony between fusiform cells (Stefanescu and Shore, 2015, 2017; Wu et al., 2016). To test
516 this possibility, spike times were binned at both 1 and 10 ms and used to generate cross-
517 correlograms of spike times. Fusiform cells were categorized based on their spiking pattern:
518 bursting neurons have >10 spikes per oscillation cycle (Fig. 9A, left), oscillating neurons have <5
519 spikes per oscillation cycle (Fig. 9B, left), and neurons that do not exhibit oscillatory activity
520 were silent. Electrically coupled neurons in some studies have shown robust spike synchrony,
521 with synchronized spikes occurring within 5 ms of one another (Dugué et al., 2009; Trenholm et
522 al., 2014). By contrast, fusiform pairs showed no evidence of such fine-scale synchrony (Fig. 9A
523 inset), likely due to their relatively weak coupling. However, in pairs where both neurons were
524 exhibiting regular high-frequency spike bursts (Fig. 9A), the resulting cross-correlograms
525 displayed coordinated 1-2 Hz spike oscillations similar to those seen in the voltage cross-

526 correlograms. The average *xcorr* for bursting pairs was 0.22 ± 0.06 (Fig. 9C; n=6 pairs). The
527 oscillations in the cross-correlograms of oscillating pairs with lower frequency spiking (Fig. 9B)
528 were much weaker, resulting in *xcorr* values close to zero (Fig. 9C; oscillating 0.02 ± 0.01, n=6
529 pairs). The lag time of the peak of these *xcorr* oscillations was similar to lag times measured
530 when correlating oscillating membrane potential, averaging 57.3 ± 12.4 ms (n=11 pairs,
531 compared to 10.5 ± 1.8 ms for voltage oscillation lag). Cross-correlation waveforms for both
532 bursting and oscillating pairs showed an average cycle width of 1012 ± 65 ms (n=11 pairs),
533 matching the subthreshold voltage oscillations of the cells. For each bursting pair, we measured
534 the spike frequency for each cell and averaged them to get the pair spike frequency. We saw a
535 strong positive linear correlation between spike *xcorr* and spike frequency (Fig. 9D; n=12 pairs,
536 R^2=0.86, p<0.0001, linear regression) (de la Rocha et al., 2007). Increased spike frequency in
537 bursting pairs may therefore increase broad-scale spike synchrony.
538
539 **Electrical coupling, synchrony, and distance**
540 The distance between somas was approximated for a subset of dual recordings. With
541 the exception of one pair with a distance of 120 µm between cells, all electrically coupled pairs
542 fell within 80 µm of one another (n=9 pairs). There was no significant linear relationship
543 between distance and coupling coefficient (n=20 pairs, R^2=0.15, p=0.097, linear regression) or
544 oscillation synchrony (n=17 pairs, R^2=0.19, p=0.119, linear regression). Considering the highly
545 detailed mapping of mouse DCN tonotopy (Muniak et al., 2013) and the relatively conserved
546 region in which paired recordings were made, it is likely that only fusiform cells within the same
547 or similar tonotopic domains were connected.

548

549 **DISCUSSION**

550 **Biophysical basis of oscillations**

551 Fusiform cells displayed 1-2 Hz subthreshold voltage oscillations that were synchronized
552 across local clusters of neurons. Given that oscillations were present in synaptic blockers and
553 that the intrinsic resonance frequency was also 1-2 Hz, oscillations and the resonance of
554 fusiform cells are likely determined by the same intrinsic mechanisms (Fransén et al., 2004).
555 Resonance is created by active and passive properties that filter low- and high-frequency
556 voltage fluctuations, respectively, resulting in a peak in the impedance curve (Hutcheon and
557 Yarom, 2000). In fusiform cells, HCN and NaP were required to produce oscillations, consistent
558 with observations made in a variety of other brain regions (Mccormick and Pape, 1990; Fransén
559 et al., 2004; Hu et al., 2009; Boehlen et al., 2013; Matsumoto-Makidono et al., 2016;
560 Stagkourakis et al., 2018). We also observed that electrical connections between fusiform cells
561 boosted oscillation power, indicating that currents generated by NaP and HCN conductances
562 spread through neighboring cells (Apostolides and Trussell, 2014). Modeling studies in other
563 brain regions show that HCN provides a depolarizing drive for the initial rising phase of the
564 oscillation which is further supported or amplified by NaP, whereas continued depolarization
565 deactivates HCN, leading to repolarization (Hutcheon et al., 1996; Dickson et al., 2000;
566 Hutcheon and Yarom, 2000; Fransén et al., 2004). This interplay of voltage-dependent
567 activation and deactivation suggests that mechanisms that control the kinetics of HCN could
568 dictate the basal oscillation frequency in DCN, with NaP regulating its amplitude.

569 The capacity to generate 1-2 Hz oscillations developed between P9 and P16, and this
570 was paralleled by maturation of other features of fusiform cell firing. Some, such as rheobase
571 and the AP threshold, rate of rise and width, are consistent with a developmental enhancement
572 of Na^+ current (Benites et al., 2023), thus explaining the lack of oscillations at younger ages. It is
573 notable that hearing in mice begins within this time frame (P12-13), suggesting that sensory
574 activity may be a driving force for electrical maturation of fusiform cells. It will be of interest
575 therefore to examine such electrical development when auditory function is compromised.
576 Other ion channel blockers had variable effects on oscillations. Although Ca^{2+} channels
577 are required for spontaneous oscillations in inferior olive and lateral olivocochlear neurons
578 (Llinás and Yarom, 1981; Matsumoto-Makidono et al., 2016; Hong et al., 2022), these did not
579 contribute to fusiform cell oscillations. Furthermore, TEA caused an increase in oscillation
580 power, likely by enhancing input resistance. Given that 10 mM TEA blocks low- and high-voltage
581 activated K^+ channels as well as KCNQ and SK channels (Monaghan et al., 2004; Johnston et al.,
582 2010), these K^+ channels are unlikely to be involved in generating oscillations, but may instead
583 indirectly regulate oscillation amplitude.
584
585 **Effect of external Ca^{2+}**
586 External Ca^{2+} had a large effect on oscillation power, likely explaining why previous
587 studies in DCN that used > 2 mM Ca^{2+} had not noted the presence of these rather striking and
588 persistent oscillations (Gardner et al., 2001; Fujino and Oertel, 2003; Manis et al., 2003;
589 Tzounopoulos et al., 2004). Similarly, recent studies (Olsen et al., 2018; Benites et al., 2023)
590 using 2 mM external Ca^{2+} also did not report oscillations. Indeed, lowering external divalent

591 concentrations seems necessary to reveal oscillations in other acute brain slice preparations:
592 Sanchez-Vives & McCormick (2000) observed the emergence of slow oscillations *in vitro*
593 matching those observed *in vivo* when they lowered external divalent concentrations in slice to
594 *in vivo* levels (specifically from 2 to 1 mM Mg^{2+} and from 2 to 1.2 mM Ca^{2+}).
595 The effect of external Ca^{2+} concentration on oscillation power in fusiform cells is two-
596 fold, depending on the range of Ca^{2+} concentration. Between 0.5 mM and 1.7 mM Ca^{2+} ,
597 oscillation power was affected by a specific action of Ca^{2+} on Na^{+} channels (Campbell and Hille,
598 1976), because higher external Ca^{2+} induced a significant positive shift in the *v50* for NaP. While
599 an effect of divalents on Na^{+} conductance is generally attributed to charge screening, given that
600 total divalent concentration was held constant, our observations cannot be solely explained by
601 divalent charge screening unless Ca^{2+} is more effective at screening Na^{+} channels than is Mg^{2+}
602 (Horn, 1999). Between 1.7 mM and 2.5 mM, however, Ca^{2+}-activated SK channel was a major
603 player that regulates the oscillation strength. Blocking SK channels preserved the oscillations
604 that would otherwise be undectable with 2.5 mM Ca^{2+}. Nevertheless, the fact that block of SK
605 channels only preserved ~50% of oscillation power suggests that other Ca^{2+}-sensitive ionic
606 conductances may also modify oscillation strength.
607
608 **Synchrony**
609 All electrically-coupled fusiform cell pairs displayed oscillation synchrony. Given the
610 weak coupling strength between fusiform cells, a similar degree of millisecond-precision spike
611 synchrony as seen in some other electrically coupled networks is unlikely (Dugué et al., 2009;
612 Trenholm et al., 2014). Furthermore, fusiform cells are likely coupled in their dendrites, which

613 are far, and thus electrically isolated, from the axon initial segment where spikes are generated
614 (Connors 2017). As such, filter properties of transmission could contribute to the lag in
615 synchrony. By contrast, single spike synchrony between fusiform cells of similar best
616 frequencies is observed *in vivo* (Voigt and Young, 1988; Gochin et al., 1989; Stefanescu and
617 Shore, 2015, 2017). Based on our results, the most likely biological source of such fine-scale
618 spike synchrony *in vivo* is shared synaptic input. Alternatively, given that neuronal pair-wise
619 correlations scale with firing rate even in uncoupled neurons (de la Rocha et al., 2007), the high
620 sound-evoked firing rate of fusiform cells *in vivo* may also promote fine-scale spike synchrony
621 independently of electrical coupling.
622
623 **Oscillations in a physiological setting**
624 The DCN processes multisensory inputs and is representative of the class of 'cerebellum-
625 like' structures (Oertel and Young, 2004). This kind of structure also includes cerebellar cortex
626 as well as the electrosensory lobe of electric fish. The fact that this unique oscillatory pattern of
627 fusiform cells only emerges after hearing onset suggests that it might play an important role in
628 processing features of auditory signals. Electrical coupling, which boosts oscillation power,
629 appeared in fusiform cells when their somas were within 80 µm of one another. According to
630 frequency maps of mouse DCN, it is likely that only fusiform cells within similar frequency
631 domains are coupled (Muniak et al., 2013). Chemical synapses located close to electrical
632 connections enable synaptic input to spread electrically between cells (Trenholm et al., 2014).
633 NaP and HCN activation by parallel fiber input also reshapes synaptic input, significantly
634 increasing the amplitude and width of the excitatory postsynaptic potential (EPSP), and

635 inducing a damped oscillation following the EPSP (Apostolides and Trussell, 2014). Because gap
636 junctions act as low-pass filters, slower EPSPs are ideal for transmission through gap junctions
637 (Bennett and Zukin, 2004). Furthermore, active dendritic conductances such as NaP amplify
638 synaptically-induced conductances (Schwindt and Crill, 1995). Oscillations would therefore
639 amplify synaptic signals in a synchronized fashion between cells. Thus, electrical coupling may
640 allow for distribution of synaptic input amongst fusiform cells that are within the same
641 frequency domain. Shared variability resulting from synchronized oscillations may work to
642 coordinate the output from a given frequency domain and therefore strengthen the perception
643 of that frequency. Interestingly, similar mechanisms have been proposed in the principal cells
644 of the gymnotiform electrosensory lobe. These neurons also feature slow voltage oscillations
645 that drive spike bursts, as well as amplification of parallel fiber inputs by NaP (Turner et al.,
646 1996; Berman et al., 2001). A proposed function for such oscillations are to provide sensory
647 filters, possibly tuned to accommodate the fish to slow environmental changes or to detect
648 beat frequencies between the fish's own electrical signals and that of its neighbors. It is
649 possible such oscillatory mechanisms in fusiform cells play a similar role in tuning to
650 environmental or self-generated sensory signals (Singla et al., 2017).

651 Further study are needed to explore the presence of oscillations in the DCN *in vivo*. Slow
652 oscillations are unlikely to drive spontaneous spike rate as fusiform cells are known to spike at
653 20-30 Hz *in vivo* (Davis and Young, 2000; Ma and Brenowitz, 2012). Fusiform cells phase-lock to
654 amplitude-modulated tones and have best envelope frequencies, but these modulation
655 frequencies are faster than 1-2 Hz (Kim et al., 1990; Rhode and Greenberg, 1994; Gdowski and
656 Voigt, 1998). The strongest evidence for slow oscillations *in vivo* is associated with spontaneous

spike bursts, which in guinea pig occurs at ~0.2 Hz (Wu et al., 2016). HCN/NaP oscillations could underlie these burst rates, particularly if more intact electrical coupling *in vivo* imposes a slower network frequency (Stagkourakis et al., 2018). Alternatively, if the conductance state of fusiform cells is higher *in vivo* than in brain slices (Fernandez et al., 2018), slow oscillations in fusiform cells may effectively be compartmentalized to dendrites and thus exert their function locally. Indeed, the distal apical dendrites of fusiform cells are likely where electrical coupling occurs, given that this is the site where they are also coupled with molecular-layer interneurons (Apostolides and Trussell, 2013).

665 **References**

666 Apostolides PF, Trussell LO (2013) Regulation of interneuron excitability by gap junction
667 coupling with principal cells. Nat Neurosci 16:1764–1772.
668 Apostolides PF, Trussell LO (2014) Control of interneuron firing by subthreshold synaptic
669 potentials in principal cells of the dorsal cochlear nucleus. Neuron 83:324–330.
670 Bakken TE et al. (2021) Comparative cellular analysis of motor cortex in human, marmoset and
671 mouse. Nature 598:111-119.
672 Beierlein M, Gibson JR, Connors BW (2000) A network of electrically coupled interneurons
673 drives synchronized inhibition in neocortex. Nat Neurosci 3:904–910.
674 Beltramo R, D'Urso G, Dal Maschio M, Farisello P, Bovetti S, Clovis Y, Lassi G, Tucci V, De PEtri
675 Tonelli D, Fellin T (2013) Layer-specific excitatory circuits differentially control recurrent
676 network dynamics in the neocortex. Nat Neurosci 16:227-234.
677 Benites NM, Rodrigues B, da Silveira CH, Kushmerick C, Leão RM (2023) Development of
678 electrophysiological properties of fusiform neurons from the dorsal cochlear nucleus of
679 mice before and after hearing onset. Journal of Neurophysiology 130:5-22.
680 Bennett MVL, Zukin RS (2004) Electrical coupling and neuronal synchronization in the
681 mammalian brain. Neuron 41:495–511.
682 Berman N, Dunn RJ, Maler L (2001) Function of NMDA receptors and persistent sodium
683 channels in a feedback pathway of the electrosensory system. J Neurophys 86:1612-1621
684 Boehlen A, Henneberger C, Heinemann U, Erchova I (2013) Contribution of near-threshold
685 currents to intrinsic oscillatory activity in rat medial entorhinal cortex layer II stellate cells.
686 J Neurophysiol 109:445–463.

Borst JGG (2010) The low synaptic release probability in vivo. Trends Neurosci 33:259–266.

Buzsáki G (2006) Rhythms of the brain. Oxford, UK: Oxford UP.

Buzsáki G, Draguhn A (2004) Neuronal oscillations in cortical networks. Science (80-) 304:1926–1930 .

Campbell DT, Hille B (1976) Kinetic and pharmacological properties of the sodium channel of frog skeletal muscle. J Gen Physiol 67:309–323.

Chen Y, Li X, Rotstein HG, Nadim F (2016) Membrane potential resonance frequency directly influences network frequency through electrical coupling. J Neurophysiol 116:1554–1563.

Connors BW (2017) Synchrony and so much more: diverse roles for electrical synapses in neural circuits. Dev Neurobiol 77:610–624.

Crochet S, Petersen CCH (2006) Correlating whisker behavior with membrane potential in barrel cortex of awake mice. Nat Neurosci 9:608–610.

Davis KA, Young ED (2000) Pharmacological evidence of inhibitory and disinhibitory neuronal circuits in dorsal cochlear nucleus. Am Physiol Soc 83:926–940.

de la Rocha J, Doirin B, Shea-Brown E, Josić K, Reyes A (2007) Correlation between neuronal spike trains increases with firing rate. Nature 448:802-807.

Dickson CT, Magistretti J, Shalinsky MH, Fransén E, Hasselmo ME, Alonso A (2000) Properties and role of Ih in the pacing of subthreshold oscillations in entorhinal cortex layer II neurons. J Neurophysiol 83:2562–2579.

Dugué GP, Brunel N, Hakim V, Schwartz E, Chat M, Lévesque M, Courtemanche R, Léna C, Dieudonné S (2009) Electrical Coupling Mediates Tunable Low-Frequency Oscillations and Resonance in the Cerebellar Golgi Cell Network. Neuron 61:126–139.

Eggermont JJ (1992) Neural interaction in cat primary auditory cortex. Dependence on recording depth, electrode separation, and age. J Neurophysiol 68:1216–1228.

Einstein MC, Plack PO, Tran DT, Golshani P (2017) Visuall evoked 3-5 Hz membrane potential oscillations reduce the responsiveness of visual cortex neurons in awake behaving mice. J Neurosci 37:5084-5098.

Feng G, Mellor RH, Bernstein M, Keller-Peck C, Nguyen QT, Wallace M, Nerbonne JM, Lichtman JW, Sanes JR (2000) Imaging neuronal sets in transgenic mice expressing multiple spectral variants of GFP. Neuron 28:41–51.

Fernandez FR, Rahsepar B, White JA (2018) Differences in the Electrophysiological Properties of Mouse Somatosensory Layer 2/3 Neurons In Vivo and Slice Stem from Intrinsic Sources Rather than a Network-Generated High Conductance State. eNeuro 5.

Frankenhaeuser B, Hodgkin A (1957) The action of calcium on the electrical properties of squid axon. J Physiol 137:218–244.

Fransén E, Alonso AA, Dickson CT, Magistretti J, Hasselmo ME (2004) Ionic mechanisms in the generation of subthreshold oscillations and action potential clustering in entorhinal layer II stellate neurons. Hippocampus 14:368–384.

Fujino K, Oertel D (2003) Bidirectional synaptic plasticity in the cerebellum-like mammalian dorsal cochlear nucleus. Proc Natl Acad Sci U S A 100:265–270.

Gardner SM, Trussell LO, Oertel D (2001) Correlation of AMPA receptor subunit composition with synaptic input in the mammalian cochlear nuclei. J Neurosci 21:7428–7437.

Gdowski GT, Voigt HF (1998) Intrinsic oscillations and discharge regularity of units in the dorsal cochlear nucleus (DCN) of the barbiturate anesthetized gerbil. Ann Biomed Eng 26:473–

487.

Gochin PM, Kaltenbach JA, Gerstein GL (1989) Coordinated activity of neuron pairs in anesthetized rat dorsal cochlear nucleus. Brain Res 497:1–11.

Guo W, Clause AR, Barth-Maron A, Polley DB (2017) A corticothalamic circuit for dynamic switching between feature detection and discrimination. Neuron 95:180-195.

Henry MJ, Hermann, B Obleser J (2016) Neural microstates govern perception of auditory input without rhythmic structure. J Neurosci 36: 860-871.

Hong H, Zeppenfeld D, Trussell LO (2022) Electrical signaling in cochlear efferents is driven by an intrinsic neuronal oscillator. Proceedings of the National Academy of Sciences of the United States of America 119:e2209565119.

Hormuzdi SG, Pais I, LeBeau FEN, Towers SK, Rozov A, Buhl EH, Whittington MA, Monyer H (2001) Impaired electrical signaling disrupts gamma frequency oscillations in connexin 36-deficient mice. Neuron 31:487–495.

Horn R (1999) The dual role of calcium: pore blocker and modulator of gating. Proc Natl Acad Sci U S A 96:3331–3332.

Hu H, Vervaeke K, Graham LJ, Storm JF (2009) Complementary theta resonance filtering by two spatially segregated mechanisms in CA1 hippocampal pyramidal neurons. J Neurosci 29:14472–14483.

Huerta PT, Lisman JE (1995) Bidirectional synaptic plasticity induced by a single burst during cholinergic theta oscillation in CA1 in vitro. Neuron 15:1053–1063.

Hughes SW, Cope DW, Blethyn KL, Crunelli V (2002) Cellular mechanisms of the slow (<1 Hz) oscillation in thalamocortical neurons in vitro. Neuron 33:947–958.

753 Hutcheon B, Miura RM, Puil E (1996) Subthreshold membrane resonance in neocortical
754 neurons. J Neurophysiol 76:683–697.
755 Hutcheon B, Yarom Y (2000) Resonance, oscillation and the intrinsic frequency preferences of
756 neurons. Trends Neurosci 23:216–222.
757 Johnston J, Forsythe ID, Kopp-Scheinpflug C (2010) Going native: voltage-gated potassium
758 channels controlling neuronal excitability. J Physiol 588:3187–3200.
759 Kanold PO, Manis PB (1999) Transient potassium currents regulate the discharge patterns of
760 dorsal cochlear nucleus pyramidal cells. J Neurosci 19:2195-2208.
761 Kim DO, Sirianni JG, Chang SO (1990) Responses of DCN-PVCN neurons and auditory nerve
762 fibers in unanesthetized decerebrate cats to AM and pure tones: Analysis with
763 autocorrelation/power-spectrum. Hear Res 45:95–113.
764 Kim Y, Trussell LO (2007) Ion channels generating complex spikes in cartwheel cells of the dorsal
765 cochlear nucleus. J Neurophysiol 97:1705–1725.
766 Kissinger ST, Pak A, Tang Y, Masmanidis SC, Chubykin AA (2018) Oscillatory encoding of visual
767 stimulus familiarity. J Neurosci 38:6223–6240.
768 Koch C (1984) Cable theory in neurons with active, linearized membranes. Biol Cybern 50:15–
769 33.
770 Lagier S, Carleton A, Lledo P-M (2004) Interplay between local GABAergic interneurons and
771 relay neurons generates oscillations in the rat olfactory bulb. J Neurosci 24:4382–4392.
772 Lakatos P, Chen CM, O'Connell MN, Mills A, Schroeder CE (2007) Neuronal oscillations and
773 multisensory interaction in primary auditory cortex. Neuron 53:279–292.
774 Lakatos P, Shah AS, Knuth KH, Ulbert I, Karmos G, Schroeder CE (2005) An oscillatory hierarchy

775 controlling neuronal excitability and stimulus processing in the auditory cortex an
776 oscillatory hierarchy controlling neuronal excitability and stimulus processing in the
777 auditory cortex. J Neurophysiol 94:1904–1911.
778 Lawrance ELA, Harper NS, Cooke JE, Schnupp JWH (2014) Temporal predictability enhances
779 auditory detection. J Acoust Soc Am 135:1–10.
780 Leao RM, Li S, Doiron B, Tzounopoulos T (2012) Diverse levels of an inwardly rectifying
781 potassium conductance generate heterogeneous neuronal behavior in a population of
782 dorsal cochlear nucleus pyramidal neurons. J Neurophysiol 107:3008–3019.
783 Llinás R, Yarom Y (1981) Electrophysiology of mammalian inferior olivary neurones in vitro.
784 Different types of voltage-dependent ionic conductances. J Physiol 315:549–567.
785 Long MA, Deans MR, Paul DL, Connors BW (2002) Rhythmicity without synchrony in the
786 electrically uncoupled inferior olive. The Journal of neuroscience : the official journal of the
787 Society for Neuroscience 22:10898-10905.
788 Ludwig A, Zong X, Jeglitsch M, Hofmann F, Biel M (1998) A family of hyperpolarization-activated
789 mammalian cation channels. Nature 393:587–591.
790 Ma W-LD, Brenowitz SD (2012) Single-neuron recordings from unanesthetized mouse dorsal
791 cochlear nucleus. J Neurophysiol 107:824–835.
792 Madisen L, Zwingman TA, Sunkin SM, Oh SW, Zariwala HA, Gu H, Ng LL, Palmiter RD, Hawrylycz
793 MJ, Jones AR, Lein ES, Zeng H (2010) A robust and high-throughput Cre reporting and
794 characterization system for the whole mouse brain. Nat Neurosci 13:133-140.

795 Manis PB (1990) Membrane properties and discharge characteristics of guinea pig dorsal
796 cochlear nucleus neurons studied in vitro. J Neurosci 10:2338-2351.
797 Manis PB, Molitor SC, Wu H (2003) Subthreshold oscillations generated by TTX-sensitive sodium
798 currents in dorsal cochlear nucleus pyramidal cells. Exp Brain Res 153:443–451.
799 Matsumoto-Makidono Y, Nakayama H, Yamasaki M, Miyazaki T, Kobayashi K, Watanabe M,
800 Kano M, Sakimura K, Hashimoto K (2016) Ionic basis for membrane potential resonance in
801 neurons of the inferior olive. Cell Rep 16:994–1004.
802 Mayer ML, Westbrook GL (1985) The action of N-methyl-d-aspartic acid on mouse spinal
803 neurones in culture. J Physiol 361:65–90.
804 Mccormick DA, Pape H (1990) Properties of a hyperpolarization-activated cation current and its
805 role in rhythmic oscillation in thalamic relay neurones. J Physiol 431:291–318.
806 Monaghan AS, Benton DC, Bahia PK, Hosseini R, Shah YA, Haylett DG, Moss GW (2004) The SK3
807 subunit of small conductance Ca^{2+}-activated K^{+} channels interacts with both SK1 and SK2
808 subunits in a heterologous expression system. J Biol Chem 279:1003-1009.
809 Muniak MA, Rivas A, Montey KL, May BJ, Francis HW, Ryugo DK (2013) 3D model of frequency
810 representation in the cochlear nucleus of the CBA/J mouse. J Comp Neurol 521:1510–
811 1532.
812 Neske GT (2016) The slow oscillation in cortical and thalamic networks: mechanisms and
813 functions. Front Neural Circuits 9:1–25.
814 Oertel D, Young ED (2004) What's a cerebellar circuit doing in the auditory system? Trends
815 Neurosci 27:104–110.
816 Okun M, Naim A, Lampl I (2010) The Subthreshold Relation between Cortical Local Field

817 Potential and Neuronal Firing Unveiled by Intracellular Recordings in Awake Rats. 30:4440–
818 4448.
819 Olsen T, Capurro A, Pilati N, Large CH, Hamann M (2018) Kv3 K+ currents contribute to spike-
820 timing in dorsal cochlear nucleus principal cells. Neuropharmacology 133:319–333.
821 Poulet JFA, Petersen CCH (2008) Internal brain state regulates membrane potential synchrony
822 in barrel cortex of behaving mice. Nature 454:881–885.
823 Puil E, Gimbarzevsky B, Miura RM (1986) Quantification of membrane properties of trigeminal
824 root ganglion neurons in guinea pigs. J Neurophysiol 55:995–1016.
825 Rhode WS, Greenberg S (1994) Encoding of amplitude modulation in the cochlear nucleus of
826 the cat. J Neurophysiol 71:1797–1825.
827 Sanchez-Vives M V., McCormick DA (2000) Cellular and network mechanisms of rhythmic
828 recurrent activity in neocortex. Nat Neurosci 3:1027–1034.
829 Schwindt PC, Crill WE (1995) Amplification of synaptic current by persistent sodium
830 conductance in apical dendrite of neocortical neurons. J Neurophysiol 74:2220–2224.
831 Singla S, Dempsey C, Warren R, Enikolopov AG, Sawtell NB (2017) A cerebellum-like circuit in
832 the auditory system cancels responses to self-generated sounds. Nat Neurosci 20:943–950.
833 Somjen GG (2004) Ions in the Brain: Normal Function, Seizures and Stroke. Oxford: Oxford UP.
834 Stagkourakis S, Pérez CT, Hellysaz A, Ammari R, Broberger C (2018) Network oscillation rules
835 imposed by species-specific electrical coupling. Elife 7:e33144.
836 Stefanescu RA, Shore SE (2015) NMDA receptors mediate stimulus-timing-dependent plasticity
837 and neural synchrony in the dorsal cochlear nucleus. Front Neural Circuits 9:1–14.
838 Stefanescu RA, Shore SE (2017) Muscarinic acetylcholine receptors control baseline activity and

839 hebbian stimulus timing-dependent plasticity in fusiform cells of the dorsal cochlear
840 nucleus. J Neurophysiol 117:1229–1238.
841 Steriade M, Contreras D, Curró Dossi R, Nuñez A (1993) The slow (< 1 Hz) oscillation in reticular
842 thalamic and thalamocortical neurons: scenario of sleep rhythm generation in interacting
843 thalamic and neocortical networks. J Neurosci 13:3284–3299.
844 Tang Z-Q, Trussell LO (2015) Serotonergic regulation of excitability of principal cells of the
845 Dorsal cochlear nucleus. J Neurosci 35:4540–4551.
846 ten Oever S, Schroeder CE, Poeppel D, Atteveldt N Van, Zion-Golumbic E (2014) Rhythmicity and
847 cross-modal temporal cues facilitate detection. Neuropsychologia 63:43–50.
848 ten Oever S, Schroeder CE, Poeppel D, van Atteveldt N, Mehta AD, Mégevand P, Groppe DM,
849 Zion-Golumbic E (2017) Low-frequency cortical oscillations entrain to subthreshold
850 rhythmic auditory stimuli. J Neurosci 37:4903–4912.
851 Trenholm S, McLaughlin AJ, Schwab DJ, Turner MH, Smith RG, Rieke F, Awatramani GB (2014)
852 Nonlinear dendritic integration of electrical and chemical synaptic inputs drives fine-scale
853 correlations. Nat Neurosci 17:1759–1766.
854 Turner RW, Plant JR, Maler L (1996) Oscillatory and burst discharge across electrosensory
855 topographic maps. J Neurophys 76: 2364-2382.
856 Tzounopoulos T, Kim Y, Oertel D, Trussell LO (2004) Cell-specific, spike timing-dependent
857 plasticities in the dorsal cochlear nucleus. Nat Neurosci 7:719–725.
858 Voigt HF, Young ED (1988) Neural correlations in the dorsal cochlear nucleus: pairs of units with
859 similar response properties. J Neurophysiol 59:1014–1032.
860 Vong L, Ye C, Yang Z, Choi B, Chua S, Jr., Lowell BB (2011) Leptin action on GABAergic neurons

861 prevents obesity and reduces inhibitory tone to POMC neurons. Neuron 71:142-154.

862 Wu C, Martel DT, Shore SE (2016) Increased synchrony and bursting of dorsal cochlear nucleus

863 fusiform cells correlate with tinnitus. J Neurosci 36:2068–2073.

864 Yaeger DB, Trussell LO (2016) Auditory Golgi cells are interconnected predominantly by

865 electrical synapses. J Neurophysiol 116:540–551.

866 Zeilhofer HU, Studler B, Arabadzisz D, Schweizer C, Ahmadi S, Layh B, Bösl MR, Fritschy JM

867 (2005) Glycinergic neurons expressing enhanced green fluorescent protein in bacterial

868 artificial chromosome transgenic mice. J Comp Neurol 482:123–141.

869

870

871 **Figure Legends**

872 **Figure 1.** Fusiform cells display 1-2 Hz spontaneous oscillations of membrane potential. **A**,
873 Example raw voltage trace from an oscillating fusiform cell in the presence of blockers of fast
874 synaptic transmission (10 µM NBQX, 10 µM MK-801, 0.5 µM strychnine and 10 µM SR-95531).
875 **B**, Power spectrum for example cell shown in **A**, with a peak between 1 and 2 Hz. **C**, Voltage
876 dependence of subthreshold oscillations (n=10 cells, power is normalized to the power
877 measured at -76 mV) in synaptic blockers. **D**, Example raw voltage trace showing oscillations in
878 the absence of synaptic blockers. **E-F**, Population data showing oscillation frequency and power
879 in control and with synaptic blockers. **G**, Population data showing the input resistance,
880 membrane capacitance and time constant (tau) in control and with synaptic blockers. *p<0.05,
881 ***p<0.001, ****p<0.0001. Error bar, SEM.

882 **Figure 2.** Oscillations are absent in P8-9 fusiform cells. **A**, Representative voltage traces from
883 fusiform cells at P8 (before hearing onset) and P17 (after hearing onset). **B**, Population data
884 showing the oscillation power in two age groups. Note that P16-25 data are the same as Figure
885 1F, right column. **C**, Population data showing input resistance, membrane capacitance and time
886 constant (tau) in two age groups. **D-E**, Raw voltage traces from the two representative neurons
887 shown in **A** in response to current injections at -200, 0 and +180 pA. Arrowhead points to the
888 delay before the first action potential. *p<0.05, ****p<0.0001. Error bar, SEM. Recordings
889 made in the presence of blockers of fast synaptic transmission (5-10 µM NBQX, 10 µM MK-801,
890 0.5-1 µM strychnine and 5-10 µM SR-95531).

891 **Figure 3.** Subthreshold oscillations require persistent Na^+ (NaP) and HCN conductances.
892 Oscillations were blocked by bath application of 0.5 µM TTX (**A**; W=11.14, p=0.0012, Friedman

893 test) and 1-2 mM CsCl (**B**; F(1.2, 10.8)=8.7, p=0.01, RM one-way ANOVA). Conversely, 10 mM
894 TEA (**C**) increased oscillation power (F=12.29, p=0.0003, Friedman test). Broad-spectrum Ca^{2+}
895 channel blockers (**D**) also appeared to increase oscillations, but the enhancement was not
896 significant (F(1.6,7.9)=4.64, p=0.052, RM one-way ANOVA). Bias current was applied to correct
897 for membrane potential changes with drug application before power measurements were
898 made. Population graphs are normalized to control. *p<0.05, **p<0.01, ***p<0.001. Error bar,
899 SEM. Recordings made in the presence of blockers of fast synaptic transmission (5-10 µM
900 NBQX, 10 µM MK-801, 0.5-1 µM strychnine and 5-10 µM SR-95531).

901 **Figure 4.** Close association between oscillation and membrane resonance. **A**, 5-pA ZAP current
902 (upper panel) elicited resonant voltage response (averaged, lower panel) from a representative
903 fusiform cell. **B**, Impedance (*Z*) from the cell shown in **A** plotted as a function of frequency. Grey
904 and black traces represent impedance curve before and after smoothing, respectively. Vertical
905 dashed line aligned at the peak of the curve. **C**, The resonance frequency of oscillating cells
906 matched the frequency of their spontaneous oscillations (t(16)=0.340, p=0.739, paired t-test).
907 **D,** Normalized impedance curve to *Z* at 0.4 Hz. The peak of this curve is defined as Q. **E,**
908 Population data showing Q values of the resonance. ****p<0.0001 as compared to 1. **F-G,**
909 Upper panel: representative voltage responses in control and after bath application of Cs^+ (1
910 mM, **F**) or TTX (1 µM, **G**). Middle panel: raw impedance curve for the voltage response shown
911 above. Lower panel: population data showing the normalized impedance curve. Vertical dashed
912 line aligned at the peak of the curve. **H,** Population data showing Q for Cs^+ or TTX. Q for drug
913 was measured as the normalized impedance in the drug, measured at the frequency where Q
914 occurred in control solutions. **p<0.01. **I,** Population data showing the *Z* ratio, calculated as

915 remaining *Z* with Cs^+ or TTX (measured at resonance frequency determined in control) divided
916 by peak *Z* in control. Error bar, SEM. Recordings made in the presence of blockers of fast
917 synaptic transmission (5-10 µM NBQX, 10 µM MK-801, 0.5-1 µM strychnine and 5-10 µM SR-
918 95531).

919 **Figure 5.** Lowering extracellular Ca^{2+} amplifies oscillations. **A**, Example raw voltage traces in
920 different external [Ca^{2+}]. **B**, Dose-response curve displaying oscillation power measured in
921 fusiform cells across varying external [Ca^{2+}] (n=8 cells). **C,** Power of oscillations from a
922 representative fusiform cell plotted as a function of time. Arrowheads point to the time when
923 the oscillations shown in the insets occurred. Note that insets are plotted in the same scale. **D**,
924 Na^+ conductance curves were measured in varying external [Ca^{2+}] by applying a 5-second ramp
925 holding from -83 to -53 mV. Raw current traces in response to the voltage ramp are displayed
926 for one cell. **E**, Boltzman curves from fits to the data in **D**. **F**, Population data comparing
927 maximum conductance, half-activation voltage, and slope measured from Boltzmann fits across
928 [Ca^{2+}]. Maximum conductance was unchanged between conditions ($F(1.2, 9.9)=1.6$, $p=0.239$,
929 RM one-way ANOVA). Half-activation voltage was positively shifted in [Ca^{2+}] greater than 0.5
930 ($F(1.7, 13.3)=31.07$, $p<0.0001$, RM one-way ANOVA). There was no significant difference in
931 slope between different external [Ca^{2+}] ($F(1.1, 9.0)=0.514$, $p=0.514$, RM one-way ANOVA).
932 *p<0.05, **p<0.01, ***p<0.001. Error bar, SEM. Recordings made in the presence of blockers of
933 fast synaptic transmission (5-10 µM NBQX, 10 µM MK-801, 0.5-1 µM strychnine and 5-10 µM
934 SR-95531).

935 **Figure 6.** Increasing extracellular Ca^{2+} concentration activates SK channels that shunt
936 oscillations. **A,** Power of oscillations from a representative fusiform cell plotted as a function of

937 time. Arrowheads point to the time when the oscillations shown in the insets occurred. Note
938 that insets are plotted in the same scale. **B,** Population data showing that the Ca^{2+} dependence
939 of input resistance (left, q(6)=6.997, p=0.006, Tukey's post hoc test) was abolished by 1 mM
940 TEA (right, q(5)=2.121, p=0.367, Tukey's post hoc test). **C-D,** Representative voltage traces
941 recorded with 1 mM TEA (**C**) or 200 nM apamin (**D**) in the bath. **E,** Population data showing that
942 the Ca^{2+} dependence of power was attenuated by application of TEA or apamin. Percent
943 reduction of power: control *vs.* TEA, q(16)=12.80, p<0.0001; control *vs.* apamin, q(16)=12.28,
944 p<0.0001, Tukey's post hoc test. *p<0.05, **p<0.01, ****p<0.0001. Error bar, SEM. Recordings
945 made in the presence of blockers of fast synaptic transmission (5-10 µM NBQX, 10 µM MK-801,
946 0.5-1 µM strychnine and 5-10 µM SR-95531).

947 **Figure 7.** Absence of effect of Ca^{2+} on HCN channel activation. **A**, Example HCN tail currents
948 (magnified in insets) measured in varying concentrations of Ca^{2+}: cells were held at -60 mV,
949 injected with current steps from -120 to -60 mV in 5 mV increments for 5 seconds, and stepped
950 back to -60 mV to induce a tail current. **B**, The HCN activation curve was generated by
951 measuring the amplitude of the resulting tail current associated with each voltage step (n=11
952 cells). Normalized population data are fit with Boltzmann sigmoid equations. **C**, The maximum
953 tail current amplitude, half-activation voltage, and slope did not vary significantly between Ca^{2+}
954 concentrations. Error bar, SEM. Recordings made in the presence of blockers of fast synaptic
955 transmission (5-10 µM NBQX, 10 µM MK-801, 0.5-1 µM strychnine and 5-10 µM SR-95531).

956 **Figure 8.** Oscillation synchrony in electrically coupled fusiform cells. **A**, Paired recordings from
957 electrically coupled fusiform cells in WT tissue. The resulting cross-correlogram for this pair,
958 shown to the right, displays a peak around zero lag. **B**, Dual recordings from two fusiform cells

959 in Cx36 KO tissue. The resulting cross-correlogram to the right shows no central peak around
960 zero lag. **C**, *Left*: Electrically coupled cells in WT tissue have significantly larger *xcorr* values
961 (measured at lag zero) than uncoupled pairs in WT and Cx36 KO tissue ($F(2,46)=49.6$, $p<0.0001$,
962 one-way ANOVA). *Right*: Lag times measured for the peak in oscillation cross-correlograms for
963 coupled pairs in WT tissue. **D**, Population statistics comparing basic features of oscillations
964 recorded from WT *vs.* Cx36 KO animals. *Left*: Oscillation power was significantly lower in
965 fusiform cells measured from Cx36 KO tissue ($U=405$, $p<0.0001$, Mann-Whitney U). *Right*: There
966 was no significant difference in oscillation frequency between WT and KO ($U=846$, $p=0.096$,
967 Mann-Whitney U). ****$p<0.0001$. Error bar, SEM. Recordings made in the presence of blockers
968 of fast synaptic transmission (5-10 µM NBQX, 10 µM MK-801, 0.5-1 µM strychnine and 5-10 µM
969 SR-95531).

970 **Figure 9.** Broad-scale spike synchrony displayed by electrically coupled fusiform cells. **A,** Paired
971 recordings from electrically coupled fusiform cells that are both *bursting* (left) and the resulting
972 spike cross-correlogram for this example pair (right). The inset displays a lack of a peak around
973 zero between ±20 ms: this indicates a lack of fine-scale spike synchrony. Indeed, no pair
974 displayed the fine-scale spike synchrony that is commonly seen in strongly electrically coupled
975 neurons of other brain regions. However, the cross-correlogram on a wider time scale shows a
976 slow oscillation matching the oscillation frequency of the neuron, indicating broad-scale spike
977 synchrony. **B,** Paired recordings from electrically coupled fusiform cells that are both *oscillating*
978 (left) and the resulting spike cross-correlogram for this example pair (right). Pairs either
979 consisted of cells that were bursting (>10 spikes per oscillation cycle), oscillating (<5 spikes per
980 oscillation cycle), or not oscillating. Oscillating pairs showed cross-correlogram oscillations

981 similar to bursting pairs, but much weaker. **C,** *xcorr* measured at zero lag for spike cross-
982 correlograms across the population of fusiform pairs. *xcorr* values measured from bursting pairs
983 were significantly larger than *xcorr* values measured from oscillating and non-oscillating pairs,
984 which both displayed *xcorr* values around 0 (W=8, p=0.01, Kruskal-Wallis). **D,** There was a
985 strong linear correlation between spike *xcorr* and spike frequency in bursting pairs (R^2=0.86,
986 p<0.0001, linear regression). Spike frequency was averaged between cells to get one value for
987 the pair. *p<0.05, ****p<0.0001. Error bar, SEM. Recordings made in the presence of blockers
988 of fast synaptic transmission (5-10 µM NBQX, 10 µM MK-801, 0.5-1 µM strychnine and 5-10 µM
989 SR-95531).

990

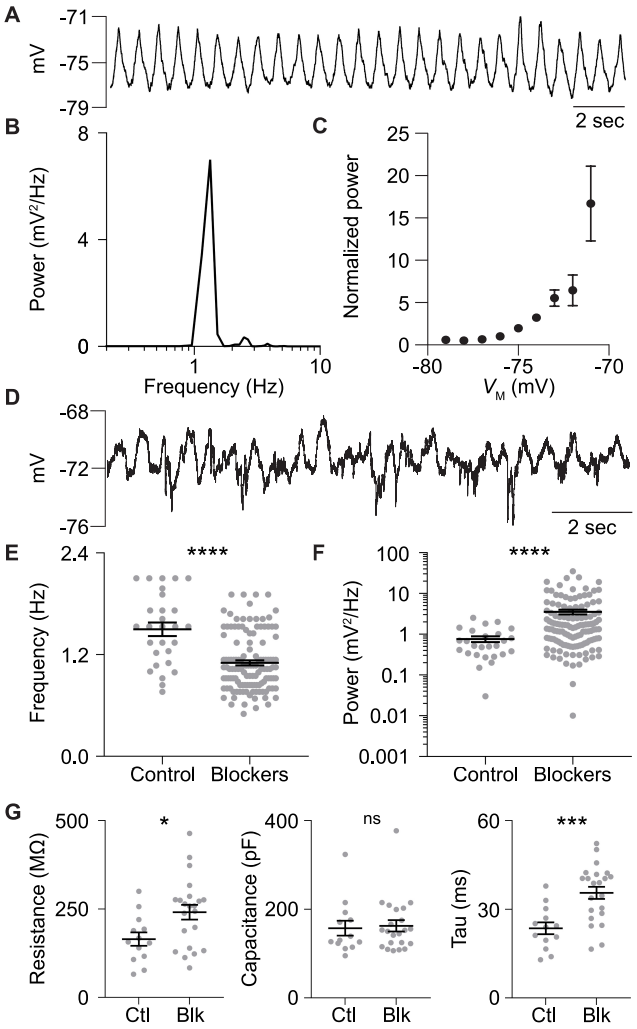

Figure 1. Fusiform cells display 1-2 Hz spontaneous oscillations of membrane potential. **A**, Example raw voltage trace from an oscillating fusiform cell in the presence of blockers of fast synaptic transmission (10 µM NBQX, 10 µM MK-801, 0.5 µM strychnine and 10 µM SR-95531). **B**, Power spectrum for example cell shown in **A**, with a peak between 1 and 2 Hz. **C**, Voltage dependence of subthreshold oscillations (n=10 cells, power is normalized to the power measured at -76 mV) in synaptic blockers. **D**, Example raw voltage trace showing oscillations in the absence of synaptic blockers. **E-F**, Population data showing oscillation frequency and power in control and with synaptic blockers. **G**, Population data showing the input resistance, membrane capacitance and time constant (tau) in control and with synaptic blockers. *p<0.05, ***p<0.001, ****p<0.0001. Error bar, SEM.

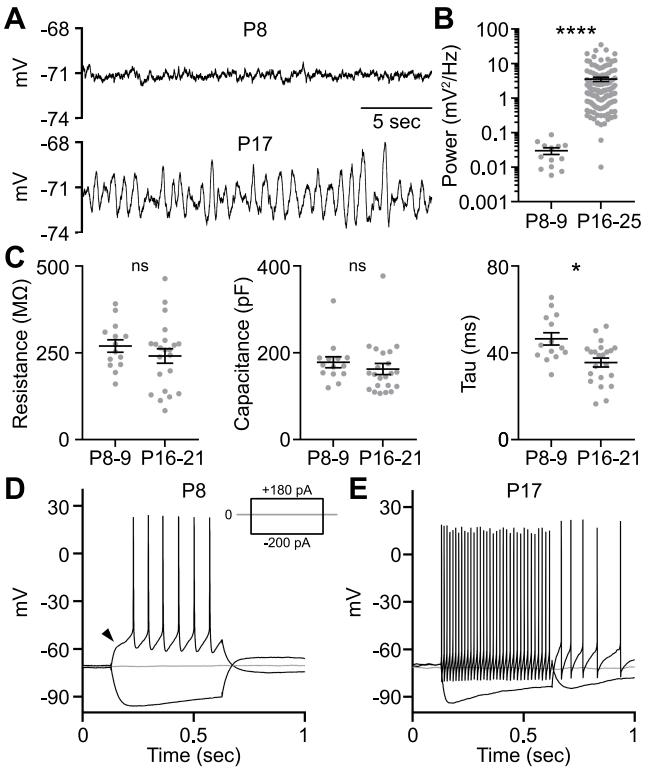

Figure 2. Oscillations are absent in P8-9 fusiform cells. **A**, Representative voltage traces from fusiform cells at P8 (before hearing onset) and P17 (after hearing onset). **B**, Population data showing the oscillation power in two age groups. Note that P16-25 data are the same as Figure 1F, right column. **C**, Population data showing input resistance, membrane capacitance and time constant (tau) in two age groups. **D-E**, Raw voltage traces from the two representative neurons shown in **A** in response to current injections at -200, 0 and +180 pA. Arrowhead points to the delay before the first action potential. *p<0.05, ****p<0.0001. Error bar, SEM. Recordings made in the presence of blockers of fast synaptic transmission (5-10 µM NBQX, 10 µM MK-801, 0.5-1 µM strychnine and 5-10 µM SR-95531).

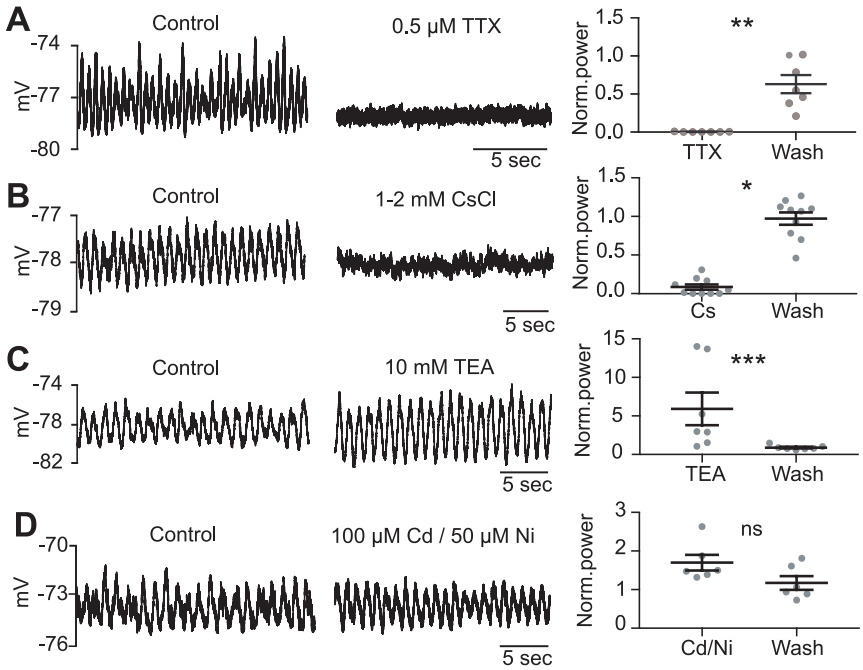

Figure 3. Subthreshold oscillations require persistent Na^+ (NaP) and HCN conductances. Oscillations were blocked by bath application of 0.5 μM TTX (**A**; W=11.14, p=0.0012, Friedman test) and 1-2 mM CsCl (**B**; F(1.2, 10.8)=8.7, p=0.01, RM one-way ANOVA). Conversely, 10 mM TEA (**C**) increased oscillation power (F=12.29, p=0.0003, Friedman test). Broad-spectrum Ca^{2+} channel blockers (**D**) also appeared to increase oscillations, but the enhancement was not significant (F(1.6,7.9)=4.64, p=0.052, RM one-way ANOVA). Bias current was applied to correct for membrane potential changes with drug application before power measurements were made. Population graphs are normalized to control. *p<0.05, **p<0.01, ***p<0.001. Error bar, SEM. Recordings made in the presence of blockers of fast synaptic transmission (5-10 μM NBQX, 10 μM MK-801, 0.5-1 μM strychnine and 5-10 μM SR-95531).

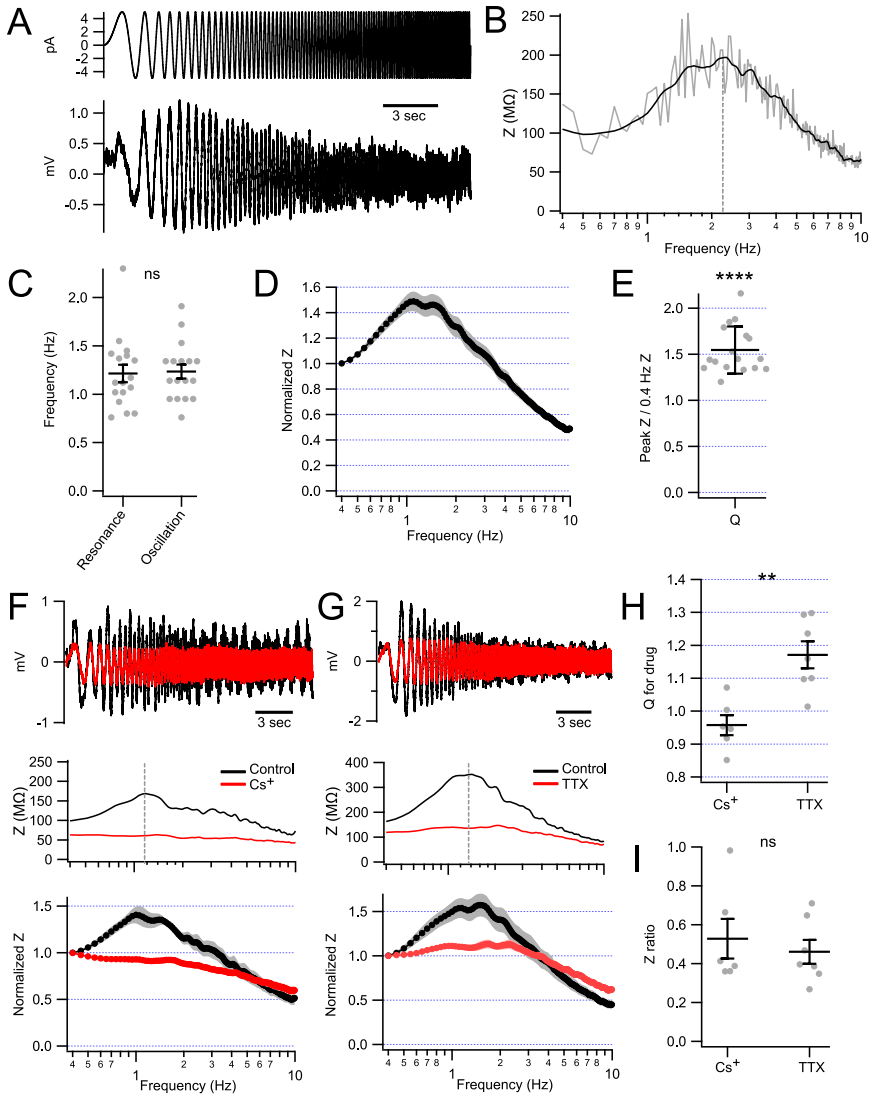

Figure 4. Close association between oscillation and membrane resonance. **A**, 5pA ZAP current (upper panel) elicited resonant voltage response (averaged, lower panel) from a representative fusiform cell. **B**, Impedance (*Z*) from the cell shown in **A** plotted as a function of frequency. Grey and black traces represent impedance curve before and after smoothing, respectively. Vertical dashed line aligned at the peak of the curve. **C**, The resonance frequency of oscillating cells matched the frequency of their spontaneous oscillations (t(16)=0.340, p=0.739, paired t-test). **D,** Normalized impedance curve to *Z* at 0.4 Hz. The peak of this curve is defined as Q. **E,** Population data showing Q values of the resonance. ****p<0.0001 as compare to 1. **F-G,** Upper panel: representative voltage responses in control and after bath application of Cs^+ (1 mM, **F**) or TTX (1 µM, **G**). Middle panel: raw impedance curve for the voltage response shown above. Lower panel: population data showing the normalized impedance curve. Vertical dashed line aligned at the peak of the curve. **H,** Population data showing Q for Cs^+ or TTX. Q for drug was measured as the normalized impedance in the drug, measured the frequency where Q occurred in control solutions. **p<0.01. **I,** Population data showing the *Z* ratio, calculated as remaining *Z* with Cs^+ or TTX (measured at resonance frequency determined in control) divided by peak *Z* in control. Error bar, SEM. Recordings made in the presence of blockers of fast synaptic transmission (5-10 µM NBQX, 10 µM MK-801, 0.5-1 µM strychnine and 5-10 µM SR-95531).

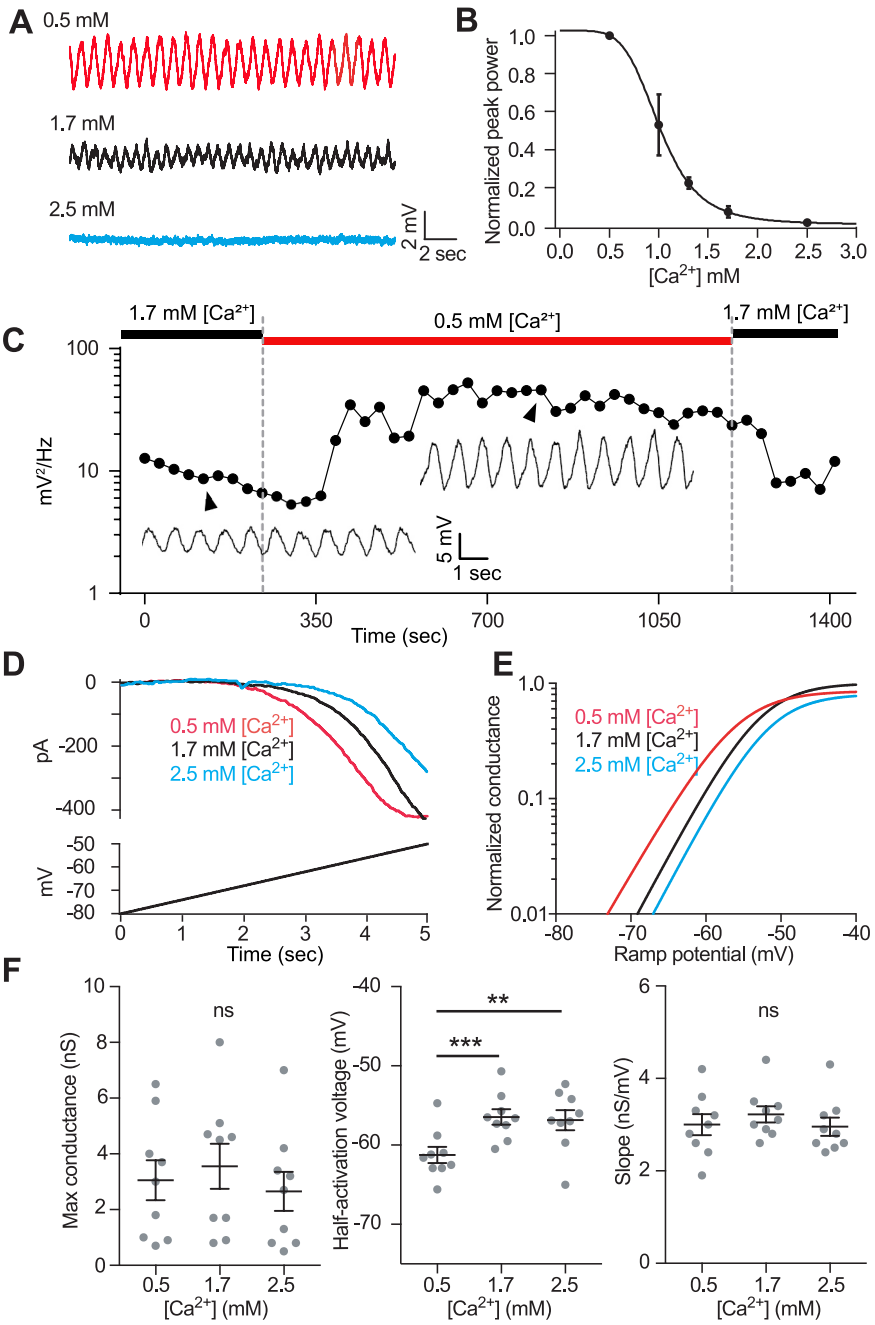

Figure 5. Lowering extracellular Ca^{2+} amplifies oscillations. **A**, Example raw voltage traces in different external [Ca^{2+}]. **B**, Dose-response curve displaying oscillation power measured in fusiform cells across varying external [Ca^{2+}] (n=8 cells). **C,** Power of oscillations from a representative fusiform cell plotted as a function of time. Arrowheads point to the time when the oscillations shown in the insets occurred. Note that insets are plotted in the same scale. **D**, Na^{+} conductance curves were measured in varying external [Ca^{2+}] by applying a 5-second ramp holding from -83 to -53 mV. Raw current traces in response to the voltage ramp are displayed for one cell. **E**, Boltzmann curves from fits to the data in **D**. **F**, Population data comparing maximum conductance, half-activation voltage, and slope measured from Boltzmann fits across [Ca^{2+}]. Maximum conductance was unchanged between conditions ($F(1.2, 9.9)=1.6$, $p=0.239$, RM one-way ANOVA). Half-activation voltage was positively shifted in [Ca^{2+}] greater than 0.5 ($F(1.7, 13.3)=31.07$, $p<0.0001$, RM one-way ANOVA). There was no significant difference in slope between different external [Ca^{2+}] ($F(1.1, 9.0)=0.514$, $p=0.514$, RM one-way ANOVA). *p<0.05, **p<0.01, ***p<0.001. Error bar, SEM. Recordings made in the presence of blockers of fast synaptic transmission (5-10 µM NBQX, 10 µM MK-801, 0.5-1 µM strychnine and 5-10 µM SR-95531).

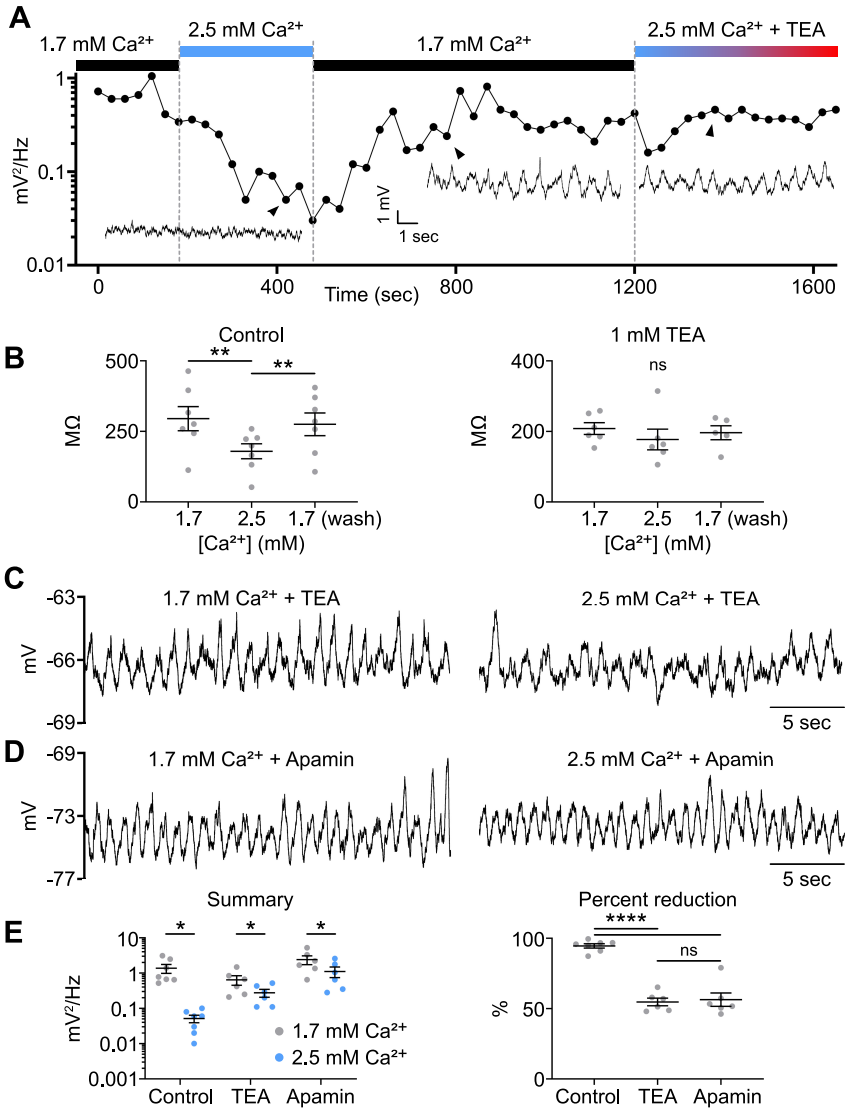

Figure 6. Increasing extracellular Ca^{2+} concentration activates SK channels that shunt oscillations. **A,** Power of oscillations from a representative fusiform cell plotted as a function of time. Arrowheads point to the time when the oscillations shown in the insets occurred. Note that insets are plotted in the same scale. **B,** Population data showing that the Ca^{2+} dependence of input resistance (left, $q(6)=6.997$, $p=0.006$, Tukey's post hoc test) was abolished by 1 mM TEA (right, $q(5)=2.121$, $p=0.367$, Tukey's post hoc test). **C-D,** Representative voltage traces recorded with 1 mM TEA (**C**) or 200 nM apamin (**D**) in the bath. **E,** Population data showing that the Ca^{2+} dependence of power was attenuated by application of TEA or apamin. Percent reduction of power: control *vs.* TEA, $q(16)=12.80$, $p<0.0001$; control *vs.* apamin, $q(16)=12.28$, $p<0.0001$, Tukey's post hoc test. *$p<0.05$, **$p<0.01$, ****$p<0.0001$. Error bar, SEM. Recordings made in the presence of blockers of fast synaptic transmission (5-10 µM NBQX, 10 µM MK-801, 0.5-1 µM strychnine and 5-10 µM SR-95531).

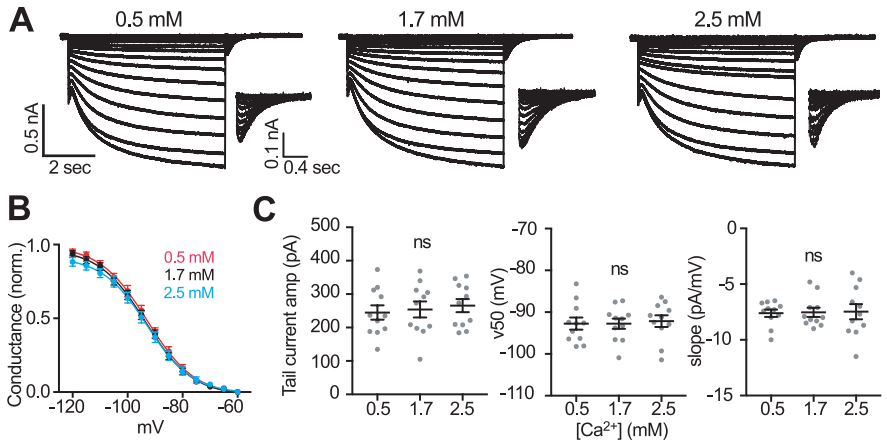

Figure 7. Absence of effect of Ca^{2+} on HCN channel activation. **A**, Example HCN tail currents (magnified in insets) measured in varying concentrations of Ca^{2+}: cells were held at -60 mV, injected with current steps from -120 to -60 mV in 5 mV increments for 5 seconds, and stepped back to -60 mV to induce a tail current. **B**, The HCN activation curve was generated by measuring the amplitude of the resulting tail current associated with each voltage step (n=11 cells). Normalized population data are fit with Boltzmann sigmoid equations. **C**, The maximum tail current amplitude, half-activation voltage, and slope did not vary significantly between Ca^{2+} concentrations. Error bar, SEM. Recordings made in the presence of blockers of fast synaptic transmission (5-10 µM NBQX, 10 µM MK-801, 0.5-1 µM strychnine and5-10 µM SR-95531).

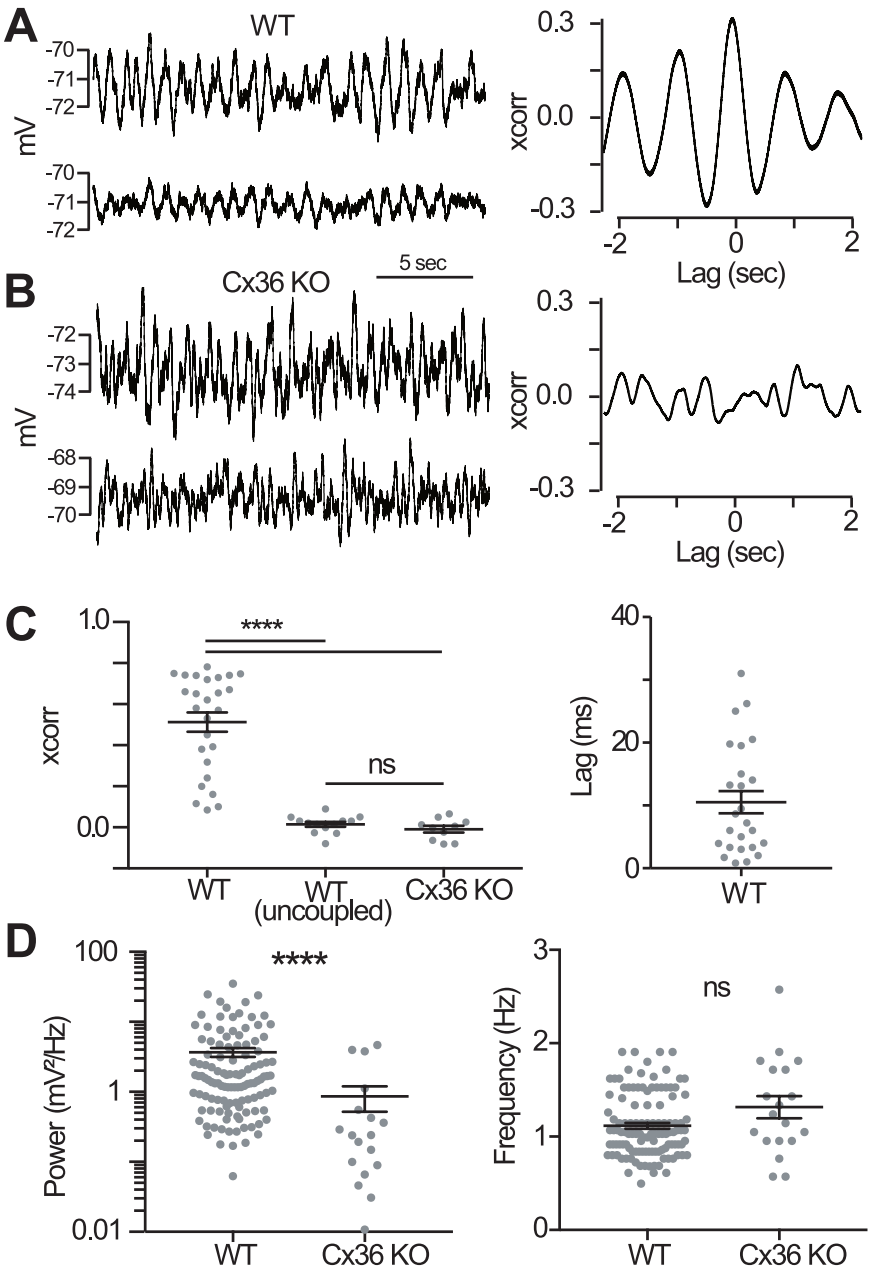

Figure 8. Oscillation synchrony in electrically coupled fusiform cells. **A**, Paired recordings from electrically coupled fusiform cells in WT tissue. The resulting cross-correlogram for this pair, shown to the right, displays a peak around zero lag. **B**, Dual recordings from two fusiform cells in Cx36 KO tissue. The resulting cross-correlogram to the right shows no central peak around zero lag. **C**, *Left*: Electrically coupled cells in WT tissue have significantly larger *xcorr* values (measured at lag zero) than uncoupled pairs in WT and Cx36 KO tissue ($F(2,46)=49.6$, $p<0.0001$, one-way ANOVA). *Right*: Lag times measured for the peak in oscillation cross-correlograms for coupled pairs in WT tissue. **D**, Population statistics comparing basic features of oscillations recorded from WT *vs.* Cx36 KO animals. *Left*: Oscillation power was significantly lower in fusiform cells measured from Cx36 KO tissue ($U=405$, $p<0.0001$, Mann-Whitney U). *Right*: There was no significant difference in oscillation frequency between WT and KO ($U=846$, $p=0.096$, Mann-Whitney U). ****$p<0.0001$. Error bar, SEM. Recordings made in the presence of blockers of fast synaptic transmission (5-10 µM NBQX, 10 µM MK-801, 0.5-1 µM strychnine and 5-10 µM SR-95531).

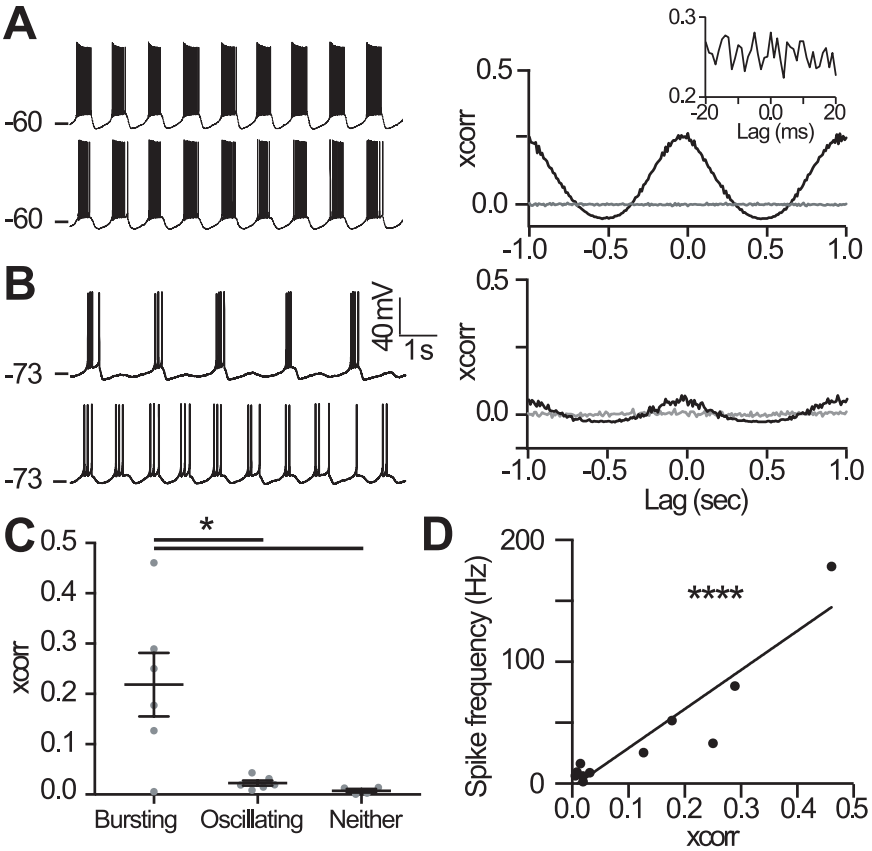

Figure 9. Broad-scale spike synchrony displayed by electrically coupled fusiform cells. **A,** Paired recordings from electrically coupled fusiform cells that are both *bursting* (left) and the resulting spike cross-correlogram for this example pair (right). The inset displays a lack of a peak around zero between ±20 ms: this indicates a lack of fine-scale spike synchrony. Indeed, no pair displayed the fine-scale spike synchrony that is commonly seen in strongly electrically coupled neurons of other brain regions. However, the cross-correlogram on a wider time scale shows a slow oscillation matching the oscillation frequency of the neuron, indicating broad-scale spike synchrony. **B,** Paired recordings from electrically coupled fusiform cells that are both *oscillating* (left) and the resulting spike cross-correlogram for this example pair (right). Pairs either consisted of cells that were bursting (>10 spikes per oscillation cycle), oscillating (<5 spikes per oscillation cycle), or not oscillating. Oscillating pairs showed cross-correlogram oscillations similar to bursting pairs, but much weaker. **C,** *xcorr* measured at zero lag for spike cross-correlograms across the population of fusiform pairs. *xcorr* values measured from bursting pairs were significantly larger than *xcorr* values measured from oscillating and non-oscillating pairs, which both displayed *xcorr* values around 0 (W=8, p=0.01, Kruskal-Wallis). **D,** There was a strong linear correlation between spike *xcorr* and spike frequency in bursting pairs (R^2=0.86, p<0.0001, linear regression). Spike frequency was averaged between cells to get one value for the pair. *p<0.05, ****p<0.0001. Error bar, SEM. Recordings made in the presence of blockers of fast synaptic transmission (5-10 µM NBQX, 10 µM MK-801, 0.5-1 µM strychnine and 5-10 µM SR-95531).

Extended Data - Table 2-1. Development of active properties in fusiform cells (mean ± SEM)

Active properties	**P8-9 (n=14 cells)**	**P16-20 (n=14 cells)**	**t (Student t test)***	**p**
# of APs[1]	11.14 ± 1.12	34.29 ± 3.37	Mann-Whitney U = 0	<0.0001
Latency to the peak of first AP (ms)[1]	81.04 ± 18.32	12.34 ± 3.63	Mann-Whitney U = 14	<0.0001
Rheobase (pA)	85.71 ± 9.93	21.34 ± 1.43	Mann-Whitney U = 1	<0.0001
AP threshold (mV)[2]	-46.02 ± 1.26	-50.70 ± 1.17	2.72	0.012
AP amplitude (mV)[3]	68.07 ± 1.15	78.59 ± 1.28	6.13	<0.0001
Overshoot (mV)[4]	22.04 ± 1.50	27.89 ± 1.21	3.04	0.005
Half width (ms)[5]	1.04 ± 0.05	0.33 ± 0.01	Mann-Whitney U = 0	<0.0001
Max. rise rate (mV/ms)[6]	231.50 ± 14.93	525.90 ± 18.16	12.52	<0.0001
After-hyperpolarization (AHP, mV)[7]	-17.08 ± 0.86	-21.36 ± 0.57	4.14	0.0003
AHP latency (ms)[8]	18.40 ± 1.59	1.22 ± 0.09	Mann-Whitney U = 0	<0.0001
AHP decay (mV)[9]	0.19 ± 0.05	2.59 ± 0.42	Mann-Whitney U = 1	<0.0001
Sag (Δ mV)[10]	7.97 ± 0.65	6.47 ± 0.95	1.31	0.203
Percent reduction of sag[10]	9.06 ± 0.70%	8.49 ± 1.20%	0.41	0.683

*if the variances of the two datasets are not equal and/or data are not normally distributed, Mann-Whitney test is used.

[1] In response to +180 pA current injection.

[2] Defined as voltage at the time point when spike dV/dt reached 5% of its peak. AP shape parameters measured at or near rheobase.

[3] From threshold to peak.

[4] Maximum voltage above zero mV.

[5] Spike width at 50% of threshold-to-peak voltage.

[6] Peak of first derivative of AP.

[7] Maximum negative voltage after the first AP, relative to threshold.

[8] Duration from spike peak to AHP peak.

[9] Decay in voltage 3 ms past AHP peak.

[10] I_H sag in response to -200 pA current injection.